Geophysical Journal International

Geophys. J. Int. (2023) **235,** 2231–2256
Advance Access publication 2023 September 12
GJI Gravity, Geodesy and Tides

https://doi.org/10.1093/gji/ggad354

A commercial finite element approach to modelling Glacial Isostatic Adjustment on spherical self-gravitating compressible earth models

Pingping Huang,[1,2] Rebekka Steffen,[3] Holger Steffen,[3] Volker Klemann,[2] Patrick Wu,[4] Wouter van der Wal,[5] Zdeněk Martinec[6,7] and Yoshiyuki Tanaka[8]

[1]*Department of Civil and Geospatial Engineering, School of Engineering, Newcastle University, Newcastle Upon Tyne NE*1 7*RU, UK.*
E-mail: pingping.huang@newcastle.ac.uk
[2]*Department* 1: *Geodesy, German Research Center for Geosciences (GFZ), Potsdam* 14473, *Germany*
[3]*Geodata Division, Lantmäteriet, Gävle* 80636, *Sweden*
[4]*Department of Geoscience, University of Calgary, Calgary T*2*N*-1*N*4, *Canada*
[5]*Faculty of Aerospace Engineering, Delft University of Technology, Delft* 2629*HS, The Netherlands*
[6]*Department of Geophysics, Dublin Institute for Advanced Studies DIAS, Dublin D*02 *Y*006*D*02, *Ireland*
[7]*Faculty of Mathematics and Physics, Charles University, Prague* 116 36, *Czech Republic*
[8]*Department of Earth and Planetary Sciences, The University of Tokyo, Tokyo* 1130033, *Japan*

Accepted 2023 September 8. Received 2023 August 28; in original form 2023 March 28

SUMMARY

This paper presents a method that modifies commercial engineering-oriented finite element packages for the modelling of Glacial Isostatic Adjustment (GIA) on a self-gravitating, compressible and spherical Earth with 3-D structures. The approach, called the iterative finite element body and surface force (FEMIBSF) approach, solves the equilibrium equation for deformation using the ABAQUS finite element package and calculates potential perturbation consistently with finite element theory, avoiding the use of spherical harmonics. The key to this approach lies in computing the mean external body forces for each finite element within the Earth and pressure on Earth's surface and core–mantle boundary (CMB). These quantities, which drive the deformation and stress perturbation of GIA but are not included in the equation of motion of commercial finite element packages, are implemented therein. The method also demonstrates how to calculate degree-1 deformation directly in the spatial domain and Earth-load system for GIA models. To validate the FEMIBSF method, loading Love numbers (LLNs) for homogeneous and layered earth models are calculated and compared with three independent GIA methodologies: the normal-mode method, the iterative body force method and the spectral-finite element method. Results show that the FEMIBSF method can accurately reproduce the unstable modes for the homogeneous compressible model and agree reasonably well with the Love number results from other methods. It is found that the accuracy of the FEMIBSF method increases with higher resolution, but a non-conformal mesh should be avoided due to creating the so-called hanging nodes. The role of a potential force at the CMB is also studied and found to only affect the long-wavelength surface potential perturbation and deformation in the viscous time regime. In conclusion, the FEMIBSF method is ready for use in realistic GIA studies, with modelled vertical and horizontal displacement rates in a disc load case showing agreement with other two GIA methods within the uncertainty level of GNSS measurements.

Key words: Creep and deformation; Loading of the Earth; Numerical modelling; Mechanics, theory and modelling; Structure of the Earth.

1 INTRODUCTION

The viscoelastic relaxation of the solid Earth to changing ice and water masses induced by climate variations is known as Glacial Isostatic Adjustment (GIA). The GIA process can be observed on Earth's surface in the form of global or regional sea-level changes, crustal rebound, gravity and geoid changes, etc. (Peltier 1998; Whitehouse 2018). Moreover, GIA has been shown to affect the rotational state of the Earth by changing polar wander and length of the day (e.g. Wu & Peltier 1984; Peltier 1998; Martinec & Hagedoorn 2014), alter the stress state of the

Earth which may lead to earthquakes and volcano activities (e.g. Steffen & Wu 2011; Peltier *et al.* 2022) and induce viscous heating in the mantle (Hanyk *et al.* 2005; Huang *et al.* 2018). Modelling GIA is important because on one hand, it can be applied to infer the viscosity profile of the Earth (e.g. Haskell 1935; Lau *et al.* 2016; Huang *et al.* 2019; Argus *et al.* 2021) and on the other hand, it can be used to reconstruct the ice-sheet history (e.g. Peltier 2004; Peltier *et al.* 2015; Lambeck *et al.* 2017). The former is vital in understanding other geodynamic processes such as mantle convection while the latter can provide an insight in understanding sea level rise, glacier stability and climate change (e.g. Whitehouse 2018; Gomez *et al*. 2010).

In most GIA studies a 1-D Earth structure is assumed, where the elastic parameters and viscosity only vary with depth (e.g. Peltier *et al.* 2015; Lau *et al.* 2016; Lambeck *et al.* 2017; Argus *et al.* 2021). However, inverse modelling with seismic, gravity, surface elevation and heat flow data (e.g. Schaeffer & Lebedev 2013; Karaoğlu & Romanowicz 2018; Priestley *et al.* 2018; Debayle *et al.* 2020; Fullea *et al.* 2021), and evidence from mineral physics and geodynamics (e.g. Dannberg *et al.* 2017) show that both Earth's elastic and viscous structures have strong lateral variations, especially in the lithosphere and upper mantle. While lateral variations in elasticity may only have a minor impact on Last Interglacial (LIG) sea levels (Austermann *et al.* 2021) or on present ocean tide loading (Huang *et al.* 2021, 2022), lateral heterogeneity in viscosity can strongly influence the present-day displacement field (e.g. Wu *et al.* 2005; Paulson *et al.* 2005; Steffen *et al*. 2006; Klemann *et al.* 2008; Gomez *et al.* 2018; Peltier *et al.* 2022), and have a significant impact on sea level during the Holocene (e.g. Austermann *et al.* 2013; Li *et al.* 2018, 2022; Yousefi *et al.* 2021) and the LIG (Austermann *et al.* 2021). On the other hand, the effect of compressibility has been shown to be significant on GIA-induced horizontal displacement (Tanaka *et al.* 2011). With increasing accuracy of space geodetic techniques such as Global Navigation Satellite System (GNSS), Very Long Baseline Interferometry (VLBI) and satellite gravimetry, for example the Gravity Recovery and Climate Experiment Follow-On (GRACE-FO) mission and emerging integrated interpretations of Earth system processes, the need for improved crustal motion predictions is rising. As such, developing 3-D and compressible GIA algorithm/code is important in improving sea level and deformation predictions. However, most 3-D compressible GIA models are dedicated software that are not publicly available. This paper follows the approach of Wu (2004) in developing a new method that is based on commercial finite-element (FE) packages (e.g. ABAQUS) that are well tested, highly efficient and the results are highly reliable. In addition, users can easily modify it for other geophysical or geodynamic studies—for example in the study of GIA-induced earthquakes (e.g. Wu & Mazzotti 2007; Steffen *et al.* 2014; Wu *et al.* 2022) and of effects of more realistic rheologies on GIA (e.g. Huang *et al.* 2018, 2019). Nevertheless, as pointed out in Wu (2004), commercial FE packages are designed for engineering purposes and not tailored for the modelling of large-scale Earth deformation, thus they need to be modified by a certain method before they can be used for GIA studies. For example, Wu (2004) used the Iterative Stress Transform (IST) method on ABAQUS to model 3-D incompressible and materially compressible self-gravitating Earths, and Wong & Wu (2019) used the Iterative Body Force (IBF) method on ABAQUS to model 1-D compressible, self-gravitating Earths. Here, we develop the iterative finite element body and surface force (FEMIBSF) method on ABAQUS to model 3-D compressible, self-gravitating Earths. The aims of this paper are: (i) to discuss the mathematical formulation of the FEMIBSF method; (ii) to show the validation of this numerical method and that spatial resolution and non-conformal grid resolution can significantly affect the accuracies of our results and (iii) to outline some applications of this method so that researchers without access to dedicated GIA 3-D compressible models can use it with commercial FE packages for studying large-scale Earth deformations. Before we address these aims, we shall give a brief overview of the development of GIA models.

Traditionally, GIA is modelled in the Laplace domain by seeking normal modes of laterally homogeneous (1-D) earth models (e.g. Peltier 1974; Wu & Peltier 1982; Tromp & Mitrovica 1999). This approach is called the normal-mode method (NMM) and has been used in the GIA community in the past decades. The applicability of NMM to laterally inhomogeneous earth models is limited though, due to mode coupling which must be solved in a non-linear eigenvalue problem (e.g. Martinec 2000; Tromp & Mitrovica 2000). Using perturbation theory, Tromp & Mitrovica (2000) linearized this problem and introduced shifts in the normal-mode decay times and eigenfunctions. On the other hand, there have been a few solutions to model GIA in the time domain. Gasperini & Sabadini (1989) as well as Kaufmann *et al.* (1997), for example, used the finite element approach to study effects of lateral heterogeneity on GIA-induced displacement. Wu (1992, 1993) and Karato & Wu (1993) used the same approach to explore postglacial rebound with power-law rheology. These attempts, however, were mostly restricted to half-space models neglecting sphericity that can only be used on a regional scale up to a few 1000 km. For spherical Earth models, Hanyk *et al.* (1996) proposed an initial-value and modal approach for compressible models with 1-D complex viscosity structures, while Martinec (2000) developed a spectral-finite element approach to the forward modelling of GIA on models with 3-D viscosity structures, which has been extended by Tanaka *et al.* (2011) to incorporate the effect of compressibility. In addition, Zhong *et al.* (2003) developed a finite element method to study GIA with 3-D spherical Earth structure, while Wu & van der Wal (2003) included the effect of self-gravity in the oceans and Geruo *et al.* (2013) extended it to consider compressibility. Finally, Latychev *et al.* (2005) proposed a finite volume formulism for GIA on 3-D earth models using elastic compressibility.

In addition to the above-mentioned spherical time-domain approaches, the finite element method proposed by Wu (2004) makes use of the commercial finite element package ABAQUS which he adapted to GIA modelling in the spherical domain. Following remarks regarding the implementation of compressibility by Bängtsson & Lund (2008), the original Iterative Stress Transform (IST) method proposed in Wu (2004) and intended for incompressible earth models was extended by Wong & Wu (2019), who proposed an Iterative Body Force (IBF) approach which implements body forces in each element and solves the mechanic equilibrium equation iteratively with ABAQUS. Compressibility in Abaqus can in principle be dealt with by explicitly specifying a gravity force and using Abaqus' geometrically non-linear formulation (Hampel *et al.* 2019). However, this approach cannot be used for spherical models (Reusen *et al.* 2023). The method in

Wong & Wu (2019) is suitable for harmonic loading and 1-D spherical models where elastic and viscous parameters vary radially. In addition, like other finite element methods (e.g. Zhong *et al.* 2003; Geruo *et al.* 2013), spherical harmonics are used there to solve Poisson's equation for the gravitational potential. Moreover, Wong & Wu (2019) and Wu (2004) did not consider the degree-1 deformation since it can cause a shift in the centre of mass (COM) of the Earth-load system and that is not permitted in commercial FE modelling packages. Here, following Wong & Wu (2019), we propose a finite element approach to GIA modelling applicable for 3-D compressible Earth models with arbitrary surface loads. By this approach, we are free from decomposing the load, displacement, and potential into spherical harmonics of different degree and order (d/o) and neglecting short wavelength components (high d/o), which is common for approaches using spherical harmonics. Furthermore, we consider deformation in the Earth-load reference frame with the origin at the instantaneous COM and calculate the degree-1 deformation by subtracting the translation of the COM (e.g. Paulson *et al.* 2005; Geruo *et al.* 2013). In addition, we take the potential stress at the CMB (Wu & Peltier 1982; Tromp & Mitrovica 1999; Martinec 2000; Zhong *et al.* 2003) into account and study its impact on surface displacement and potential perturbation. Finally, the method presented here has the ability of implementing adaptive meshing (with a high resolution in the region of interest, such as the area with ice-water masses and the area with significant contrast in material properties, and a low resolution in regions of no interest, see Section 6), which is important in reducing computational cost while maintaining reasonable accuracy in numerical solutions.

In Section 2 and Appendices A and B, we present the detailed finite element method for computing radial displacement and dilatation, calculating the body and surface forces that are implemented in ABAQUS and solving Poisson's equation for the gravitational potential. We also discuss the impact of the fluid core on static deformation of the Earth and show how to consider the degree-1 deformation in the COM frame. In Section 3, we discuss the difference in the iteration scheme between our method and that in Wong & Wu (2019). The computational efficiency of FEMIBSF which uses parallel computing is evaluated in Section 4. A validation of our results is presented in Section 5 where we compare our results for homogeneous and layered 1-D earth models with those from other established methods. Resolution tests and the influence of non-conformal mesh are also shown in this section. Applications of FEMIBSF in investigating the effect of a CMB potential force and a disc load example are discussed in Section 6. Conclusions are presented in Section 7. A potential implementation of rotational feedback with FEMIBSF is presented in Appendix C.

2 MATHEMATICAL FORMULATION

The mathematical equations introduced in Wong & Wu (2019) such as the interpolation and integration equations based on an axisymmetric element and the usage of zonal harmonics, are applicable for 1-D earth models. To adapt to 3-D earth models, the classical finite element (FE) equations (e.g. Zienkiewicz *et al.* 2005) based on 3-D isoparametric elements are used here and reviewed in Appendices A and B. There, we introduce two coordinate systems: one is a spherical system L_k (r, θ, φ) and the other is a Cartesian system R_k (g, h, s) (Fig. A1). The equations in the Appendices are applied to compute the geometric area, volume, displacement, dilatation, surface/body forces and gravitational potential perturbation as well as the degree-1 deformation which are specific to GIA. In particular, by using the classical FE techniques, we avoid the usage of spherical harmonics and so avoid the leakage of high-degree load contribution (Section 2.3). Therefore, explicitly introducing these equations are beneficial for readers.

2.1 Compressibility and dilatation

The compressibility of solid Earth material results in dilatation, which further causes mass anomalies in Earth's interior that contribute to gravitational potential perturbations (Section 2.3). Thus, it requires specific mathematical treatment**.** The definition of dilatation is straightforward in L_k, that is

$$\nabla \cdot \boldsymbol{u} = \frac{\partial u_x}{\partial x} + \frac{\partial u_y}{\partial y} + \frac{\partial u_z}{\partial z}. \tag{2.1.1}$$

Here, $\boldsymbol{u}$ is the displacement vector and u_x, u_y and u_z are its x, y and z component, respectively. Evaluating $\partial u_x/\partial x$, $\partial u_y/\partial y$ and $\partial u_z/\partial z$ is not straightforward but needs making use of eq. (B2). With some algebra manipulation, one can get

$$\frac{\partial u_x}{\partial x} = \frac{1}{\|J_V\|}\begin{vmatrix} \frac{\partial u_x}{\partial g} & \frac{\partial y}{\partial g} & \frac{\partial z}{\partial g} \\ \frac{\partial u_x}{\partial h} & \frac{\partial y}{\partial h} & \frac{\partial z}{\partial h} \\ \frac{\partial u_x}{\partial s} & \frac{\partial y}{\partial s} & \frac{\partial z}{\partial s} \end{vmatrix},$$

$$\frac{\partial u_y}{\partial y} = \frac{1}{\|J_V\|}\begin{vmatrix} \frac{\partial x}{\partial g} & \frac{\partial u_y}{\partial g} & \frac{\partial z}{\partial g} \\ \frac{\partial x}{\partial h} & \frac{\partial u_y}{\partial h} & \frac{\partial z}{\partial h} \\ \frac{\partial x}{\partial s} & \frac{\partial u_y}{\partial s} & \frac{\partial z}{\partial s} \end{vmatrix},$$

and

$$\frac{\partial u_z}{\partial z} = \frac{1}{\|J_V\|}\begin{vmatrix} \frac{\partial x}{\partial g} & \frac{\partial y}{\partial g} & \frac{\partial u_z}{\partial g} \\ \frac{\partial x}{\partial h} & \frac{\partial y}{\partial h} & \frac{\partial u_z}{\partial h} \\ \frac{\partial x}{\partial s} & \frac{\partial y}{\partial s} & \frac{\partial u_z}{\partial s} \end{vmatrix} \tag{2.1.2}$$

where J_v is the Jacobian matrix (eq. A9) and the derivative of $x/y/z$ with respect to $g/h/s$ is given in Appendix A.

2.2. The density and Eulerian potential perturbations

The GIA-related density perturbations involve two types: one is due to surface mass (ice and water mass) redistribution and the other due to internal mass redistribution caused by the deformation. Denoting the surface mass density by σ, then the total surface mass reads as

$$\iint \sigma \, \mathrm{d}S' = \iint \left(\int_0^\infty \sigma \delta \left(r' - a \right) \, \mathrm{d}r' \right) \mathrm{d}S', \tag{2.2.1}$$

where the integral on the left-hand side is with respect to the Earth's surface and can be transformed into the integral on the right-hand side involving the whole Earth's volume. It follows from the right-hand side integration that an equivalent volume mass density of the surface load is

$$\rho_s = \sigma \left(\theta', \varphi' \right) \delta \left(r' - a \right). \tag{2.2.2}$$

The density perturbation in the Earth's interior, based on the conservation of mass, reads (Wu & Peltier 1982; Tromp & Mitrovica 1999; Martinec 2000)

$$\rho_1 \left(\boldsymbol{r'} \right) = -\nabla \cdot \left(\rho_0 \, \boldsymbol{u} \right). \tag{2.2.3}$$

For an earth model with a layered structure, the initial density can be expressed as (Geruo *et al.* 2013)

$$\rho_0 \left(r' \right) = \sum_{j=1}^{N} \Delta \rho^j H \left(r'_j - r' \right), \tag{2.2.4}$$

where N is the number of layers and H is the Heaviside function. For the jth layer with an upper-bound radius r_j and lower-bound r_{j-1}, the density is ρ^{j}. $\Delta\rho^{\mathrm{j}}$ denotes the density jump at r_j from the $(j+1)$th layer to the jth layer, that is

$$\Delta \rho^j = \rho^j - \rho^{j+1} \text{ for } j = 1, 2, \ldots, N \text{ from the CMB to the surface of the Earth.} \tag{2.2.5}$$

Note that $\rho^{\mathrm{N+1}}$ denotes the density outside the Earth which equals to 0 while ρ^1 is the density of the core. Substituting eq. (2.2.4) into eq. (2.2.3), one can obtain (Geruo *et al.* 2013)

$$\rho_1 \left(\boldsymbol{r'} \right) = \sum_{j=1}^{N} \Delta \rho^j \delta \left(r'_j - r' \right) \, u_{\,r} - \rho_0 \nabla \cdot \boldsymbol{u}. \tag{2.2.6}$$

The potential perturbation (ϕ_1) induced by surface and internal density anomalies, complies with the Poisson's equation

$$\nabla^2 \phi_1 = 4\pi G \left(\rho_1 + \rho_s \right) \tag{2.2.7}$$

The solution to ϕ_1, with the application of Green's function method, is given by

$$\phi_1 \left(\boldsymbol{r} \right) = - \iiint \frac{G}{|\boldsymbol{r} - \boldsymbol{r'}|} \left(\rho_1 \left(\boldsymbol{r'} \right) + \rho_s \right) \mathrm{d}V' \tag{2.2.8}$$

Substituting eqs (2.2.2) and (2.2.6) into eq. (2.2.8), one can get (Wu 2004; Geruo *et al.* 2013)

$$\phi_1 \left(\boldsymbol{r} \right) = - \sum\nolimits_{j=1}^{N} \iint \frac{G}{|\boldsymbol{r} - \boldsymbol{r'}|} \Delta \rho^j u_r \left(\boldsymbol{r}'_j \right) \mathrm{d}S' + \iiint \frac{G}{|\boldsymbol{r} - \boldsymbol{r'}|} \rho_0 \left(\nabla \cdot \boldsymbol{u} \right) \mathrm{d}V' - \iint \frac{G}{|\boldsymbol{r} - \boldsymbol{a'}|} \sigma \, \mathrm{d}S', \tag{2.2.9}$$

where a' is the radius of the Earth. Inspection of eq. (2.2.9) shows that the potential perturbation is induced by the load (the third term on the right), dilatation (the second term on the right) and radial displacement related to internal boundaries (the first term on the right). The load potential ϕ_2 (the third term) plays a role through the gravitational body force in inducing deformation and thus deformational potential (the sum of the first and second terms) ϕ_3. As such, ϕ_2 can also be called the driving potential and ϕ_3 the responding potential. It is well known that the driving and responding potentials cancel each other in the isostatic (fluid) limit and thus the total potential ϕ_1 vanishes.

Alternatively, the Eulerian potential perturbation can be obtained by solving Poisson's equation subject to boundary conditions (e.g. Tromp & Mitrovica 1999; Latychev *et al.* 2005; Martinec & Hagedoorn 2014). Poisson's equation differs from eq. (2.2.7) by vanishing ρ_s. The boundary conditions on the external boundary (Earth's surface) are

$$[\phi_1]^+_- = 0$$

and

$$[\boldsymbol{e_r} \cdot \nabla \phi_1]^+_- = 4\pi G \rho_0 \, u_r + 4\pi G \sigma, \tag{2.2.10}$$

where $+$ and $-$ denote the upper and lower side of a boundary, respectively, and $\boldsymbol{e_r}$ is the unit vector perpendicular to the boundary and pointing outside of the domain. The boundary conditions on the internal boundaries and core–mantle boundary (CMB) are

$$[\phi_1]^+_- = 0$$

and

$$[\boldsymbol{e_r} \cdot \nabla \phi_1]^+_- = -4\pi G u_r \, [\rho_0]^+_-. \tag{2.2.11}$$

Applying the Green's function method to solve Poisson's equation subject to boundary conditions (eqs 2.2.10 and 2.2.11), one can obtain the solution

$$\phi_1(\boldsymbol{r}) = -\iiint \frac{G}{|\boldsymbol{r}-\boldsymbol{r}'|}\rho_1(\boldsymbol{r}')\,\mathrm{d}V' + \sum_{j=1}^{N}\iint \frac{G}{|\boldsymbol{r}-\boldsymbol{r}'|}[\rho_0]_-^+ u_r\left(\boldsymbol{r}'_j\right)\,\mathrm{d}S'. \tag{2.2.12}$$

Substituting eq. (2.2.6) into eq. (2.2.12) and applying Gauss's integration theory, one can get

$$\phi_1(\boldsymbol{r}) = -\iint \frac{G}{|\boldsymbol{r}-\boldsymbol{b}'|}\rho_c u_r(\boldsymbol{b}')\,\mathrm{d}S' - \iiint \frac{G}{|\boldsymbol{r}-\boldsymbol{r}'|^3}\rho_0\boldsymbol{u}\cdot(\boldsymbol{r}-\boldsymbol{r}')\,\mathrm{d}V' - \iint \frac{G}{|\boldsymbol{r}-\boldsymbol{a}'|}\sigma\,\mathrm{d}S', \tag{2.2.13}$$

where b' is the radius of the CMB and ρ_c is the density of the fluid core. Note that eq. (2.3.13) is identical to eq. (14) of Latychev *et al.* (2005) and equivalent to eq. (2.2.9). As pointed out by Latychev *et al.* (2005), the density anomaly at the CMB from the core side is $\rho_c\, u_r$ (eq. 12 of Latychev *et al.* 2005), the only contribution of the fluid core to the gravitational perturbation ϕ_1. The integration domain in both eq. (2.2.9) and eq. (2.2.13) is from the CMB to the Earth's surface because we assume an incompressible and uniform fluid core which has no volumetric density perturbation under static deformation (see Section 2.4).

In practice, we calculate ϕ_1 at each node with the two-point Gauss–Legendre quadrature rule after transforming all integrals in eq. (2.2.9) or eq. (2.2.13) into the R_k coordinate system, a procedure demonstrated by eqs (A4) to (A10). The ϕ_1 value inside the element and their derivatives can be obtained again with the trilinear interpolation method. Compared to the spectral method used to compute ϕ_1 (e.g. Zhong *et al.* 2003; Wu 2004; Geruo *et al.* 2013; Wong & Wu 2019), our direct integration method (a similar method is used in Wang & Li (2021) for mantle convection modelling) gets rid of spherical harmonics and so avoids the leakage of high-degree load contribution. Moreover, with the direct integration method, the displacement output in the spatial domain can be directly used to compute the potential, whereas with the spectral method the spatial-domain displacement needs to be decomposed into spherical harmonics which are then used to reconstruct the potential. However, the direct integration method involves integration of all 3-D elements constructing the Earth model, which makes the computational load heavy. Therefore, it is difficult to confirm which method is more computationally efficient. Using a parallel computation scheme, the speed of direct integration can be increased significantly, as will be demonstrated in Section 3.

2.3. The Iterative FEMIBSF approach

2.3.1 The equilibrium equation

During glacial isostatic adjustment, the surface load exerts gravitational forces inside the Earth and pressure on Earth's surface, which makes the Earth deform. Considering the small magnitude of acceleration, the Earth is assumed to be in a mechanical equilibrium state where the total forces acting on any portion of the viscoelastic body must vanish. The equilibrium equation reads (Peltier 1974; Wu & Peltier 1982)

$$\nabla\cdot\boldsymbol{\tau} - \rho_0\nabla(g_0 u_r) - \rho_0\nabla\phi_1 + \rho_0 g_0(\nabla\cdot\boldsymbol{u})\,\boldsymbol{e_r} = 0, \tag{2.3.1}$$

and holds pointwise. The associated body forces in eq. (2.3.1) include the force exerted by internal stress perturbation (the first term), the force due to pre-stress advection (the second term), the gravitational forces due to perturbation in the gravity field (the third term) and due to the density perturbation induced by compressibility (the fourth term). The equilibrium equation is subject to the boundary condition on stresses acting on external boundaries of our solution domain including the mantle and lithosphere. Let τ_{rr} be the stress in the radial direction. Then at the Earth's surface (ES), the surface loads induce a stress which is (Wu & Peltier 1982; Wu 2004; Wong & Wu 2019)

$$\tau_{rr}^{\mathrm{ES}} = -\sigma g. \tag{2.3.2}$$

At the CMB, the stress consists of a potential force (i.e. potential stress, the first term in eq. 2.3.3), and a buoyancy from the core (the second term in eq. 2.3.3) (Wu & Peltier 1982; Tromp & Mitrovica 1999; Martinec 2000; Zhong *et al.* 2003), that is

$$\tau_{rr}^{\mathrm{CMB}} = \rho_c\phi_1 + \rho_c g_0 u_r. \tag{2.3.3}$$

The latter three body forces in eq. (2.3.1), together with the two surface forces in eqs (2.3.2) and (2.3.3), are called external or driving forces which cause the static deformation and stress perturbation in Earth's mantle and lithosphere. We use a commercial FE package (e.g. ABAQUS) to solve the equilibrium equation (eq. 2.3.1) for displacement subject to boundary conditions (eqs 2.3.2 and 2.3.3). Therefore, these external forces must be specified in each iteration/step when using commercial FE packages. Wong & Wu (2019) were the first to apply this idea to GIA modelling, where they called it the iterative body force (IBF) approach with the role of surface forces neglected. Here, to supplement the role of surface forces in the finite element method, we rename this approach as iterative FEMIBSF approach.

In addition, in Appendix C we show how the rotational feedback of GIA can potentially be implemented with FEMIBSF.

2.3.2 Evaluating the external body forces

As the element is at the heart of the finite element approach, eq. (2.3.1) is not solved pointwise but for each individual element. This means we need to consider and specify the total external forces acting on each element. ABAQUS provides an easy way to achieve this goal: the

user only needs to specify the average external body force for each element, plus the pressure (stress) for elements on external boundaries. Therefore, our task now is to compute the mean body force and pressure, which is done by applying the finite element equations in Appendices A and B.

Based on eq. (2.3.1), we define a scalar f as

$$f = -\rho_0 g_0 u_r - \rho_0 \phi_1. \tag{2.3.4}$$

The derivatives of f with respect to spatial coordinates g, h and s are

$$\begin{bmatrix} \frac{\partial f}{\partial g} \\ \frac{\partial f}{\partial h} \\ \frac{\partial f}{\partial s} \end{bmatrix} = \begin{bmatrix} \frac{\partial g_0}{\partial g} & \frac{\partial u_r}{\partial g} & \frac{\partial \phi_1}{\partial g} \\ \frac{\partial g_0}{\partial h} & \frac{\partial u_r}{\partial h} & \frac{\partial \phi_1}{\partial h} \\ \frac{\partial g_0}{\partial s} & \frac{\partial u_r}{\partial s} & \frac{\partial \phi_1}{\partial s} \end{bmatrix} \begin{bmatrix} -\rho_0 u_r \\ -\rho_0 g_0 \\ -\rho_0 \end{bmatrix} \tag{2.3.5}$$

with the assumption that ρ_0 is a constant within the element. Evaluating eq. (2.3.5) requires computing the derivatives of initial gravity, radial displacement and potential perturbation in the R_k coordinate system. The latter two derivatives are given in Appendix B and Section 2.2. For the initial gravity, we compute its value at each node with radius r ($r_{j-1} < r \leq r_j$) by the analytical expression (Martinec 2000)

$$g_0(r) = \frac{4\pi G}{3}\left(\rho^j r + \frac{R_j}{r^2}\right), \tag{2.3.6}$$

where

$$R_j = \begin{cases} 0 \quad for\ j = 1 \\ \sum_{i=2}^{j} \Delta\rho_{i-1} r_{i-1}^3 \quad for\ j = 2, \cdots, N \end{cases}.$$

The initial gravity and its derivatives inside the element are interpolated in the R_k system (see Appendix A and Fig. A1) by

$$g_0(g,h,s) = \sum_{i=1}^{8} N_i(g,h,s)\, g_{0i} \tag{2.3.7}$$

and

$$\frac{\partial g_0}{\partial g} = \sum_{i=1}^{8} \frac{\partial N_i}{\partial g} g_{0i}, \quad \frac{\partial g_0}{\partial h} = \sum_{i=1}^{8} \frac{\partial N_i}{\partial h} g_{0i}, \quad \frac{\partial g_0}{\partial s} = \sum_{i=1}^{8} \frac{\partial N_i}{\partial s} g_{0i}, \tag{2.3.8}$$

respectively.

We now evaluate the 1st and 2nd body forces in eq. (2.3.1). Since u_r and ϕ_1 depend on x, y and z, it follows that the pointwise body force is

$$\boldsymbol{F}_{12} = \nabla f = \frac{\partial f}{\partial x}\boldsymbol{e_x} + \frac{\partial f}{\partial y}\boldsymbol{e_y} + \frac{\partial f}{\partial z}\boldsymbol{e_z}. \tag{2.3.9}$$

Here, $\partial f/\partial x$, $\partial f/\partial y$ and $\partial f/\partial z$ are the x, y and z component of $\boldsymbol{F_{12}}$, respectively. The mean body force for an individual element can be calculated in the R_k system by

$$\langle F_{12x}\rangle = \frac{1}{V_k}\iiint \frac{\partial f}{\partial x} d\Omega = \frac{1}{V_k}\int_{-1}^{1}\int_{-1}^{1}\int_{-1}^{1} \frac{\partial f}{\partial x} |J_V|\, dh\, dg\, ds$$
$$\langle F_{12y}\rangle = \frac{1}{V_k}\int_{-1}^{1}\int_{-1}^{1}\int_{-1}^{1} \frac{\partial f}{\partial y} |J_V|\, dh\, dg\, ds,$$

and

$$\langle F_{12z}\rangle = \frac{1}{V_k}\int_{-1}^{1}\int_{-1}^{1}\int_{-1}^{1} \frac{\partial f}{\partial z} |J_V|\, \mathrm{d}h\, \mathrm{d}g\, \mathrm{d}s, \tag{2.3.10}$$

where

$$\frac{\partial f}{\partial x} = \frac{1}{|J_V|}\begin{vmatrix} \frac{\partial f}{\partial g} & \frac{\partial y}{\partial g} & \frac{\partial z}{\partial g} \\ \frac{\partial f}{\partial h} & \frac{\partial y}{\partial h} & \frac{\partial z}{\partial h} \\ \frac{\partial f}{\partial s} & \frac{\partial y}{\partial s} & \frac{\partial z}{\partial s} \end{vmatrix},$$
$$\frac{\partial f}{\partial y} = \frac{1}{|J_V|}\begin{vmatrix} \frac{\partial x}{\partial g} & \frac{\partial f}{\partial g} & \frac{\partial z}{\partial g} \\ \frac{\partial x}{\partial h} & \frac{\partial f}{\partial h} & \frac{\partial z}{\partial h} \\ \frac{\partial x}{\partial s} & \frac{\partial f}{\partial s} & \frac{\partial z}{\partial s} \end{vmatrix},$$

and

$$\frac{\partial f}{\partial z} = \frac{1}{|J_V|}\begin{vmatrix} \frac{\partial x}{\partial g} & \frac{\partial y}{\partial g} & \frac{\partial f}{\partial g} \\ \frac{\partial x}{\partial h} & \frac{\partial y}{\partial h} & \frac{\partial f}{\partial h} \\ \frac{\partial x}{\partial s} & \frac{\partial y}{\partial s} & \frac{\partial f}{\partial s} \end{vmatrix}. \tag{2.3.11}$$

Similarly, based on eq. (2.3.1), we define the third pointwise body force

$$\boldsymbol{F}_3 = \rho_0 g_0 (\nabla \cdot \boldsymbol{u})\, \boldsymbol{e}_r. \tag{2.3.12}$$

Expressing $\boldsymbol{e}_r$ by $\boldsymbol{e}_x$, $\boldsymbol{e}_y$ and $\boldsymbol{e}_z$, one can get the x, y and z component of $\boldsymbol{F}_3$ which reads as

$$\begin{aligned} F_{3x} &= \frac{\rho_0 g_0 (\nabla \cdot \boldsymbol{u})\, x}{\sqrt{x^2+y^2+z^2}}, \\ F_{3y} &= \frac{\rho_0 g_0 (\nabla \cdot \boldsymbol{u})\, y}{\sqrt{x^2+y^2+z^2}}, \\ F_{3z} &= \frac{\rho_0 g_0 (\nabla \cdot \boldsymbol{u})\, z}{\sqrt{x^2+y^2+z^2}}, \end{aligned} \tag{2.3.13}$$

respectively.

Accordingly, the mean $\boldsymbol{F}_3$ for an individual element expressed in R_k is given by

$$\begin{aligned} \langle F_{3x} \rangle &= \frac{1}{V_k} \iiint F_{3x}(x, y, z)\, d\Omega = \frac{1}{V_k} \int_{-1}^{1}\int_{-1}^{1}\int_{-1}^{1} F_{3x} |J_V|\, dh\, dg\, ds \\ \langle F_{3y} \rangle &= \frac{1}{V_k} \int_{-1}^{1}\int_{-1}^{1}\int_{-1}^{1} F_{3y} |J_V|\, dh\, dg\, ds \\ \langle F_{3z} \rangle &= \frac{1}{V_k} \int_{-1}^{1}\int_{-1}^{1}\int_{-1}^{1} F_{3z} |J_V|\, \mathrm{d}h\, \mathrm{d}g\, \mathrm{d}s. \end{aligned} \tag{2.3.14}$$

The integrals in eqs (2.3.10) and (2.3.14) are evaluated again with the two-point Gauss–Legendre quadrature rule. The sum of $\boldsymbol{F}_{12}$ and $\boldsymbol{F}_3$ is implemented as a uniform body force in ABAQUS.

2.3.3 Evaluating the pressure

ABAQUS takes the convention that the pressure has an opposite sign to that of the stress. Based on eq. (2.3.2), the pressure on Earth's surface is

$$P = \sigma g_0. \tag{2.3.15}$$

Here, we interpolate the initial gravity and surface mass density within the surface element by

$$\begin{aligned} g_0 &= \sum_{i=1}^{4} N_i(g, h)\, g_{0i}, \\ \sigma &= \sum_{i=1}^{4} N_i(g, h)\, \sigma_i, \end{aligned} \tag{2.3.16}$$

where g_{0i} and σ_i are nodal values. The average pressure over an elemental surface is given by

$$\langle P \rangle = \langle \sigma g_0 \rangle = \frac{1}{S_k} \int_{-1}^{1}\int_{-1}^{1} \sigma g_0 |J_S|\, \mathrm{d}g\, \mathrm{d}h. \tag{2.3.17}$$

Similarly, on the CMB the pressure from the fluid core, based on eq. (2.3.3), is

$$P = -\rho_c \phi_1 - \rho_c g_0 u_r. \tag{2.3.18}$$

The second term on the right can be modelled by Winkler foundations ($\rho_c g_0$) in ABAQUS (Wu 2004; Wong & Wu 2019). The first term on the right is modelled by prescribing the mean pressure as

$$\langle -\rho_c \phi_1 \rangle = \frac{1}{S_k} \int_{-1}^{1}\int_{-1}^{1} (-\rho_c \phi_1) |J_S|\, \mathrm{d}g\, \mathrm{d}h. \tag{2.3.19}$$

The integrals in eqs (2.3.17) and (2.3.19) are again evaluated with the two-point Gauss–Legendre quadrature rule. The mean pressure is prescribed in ABAQUS by a P2-type and P1-type pressure on elements located at the Earth's surface and CMB, respectively.

2.4. The fluid core

The role of a fluid core on static deformation of the Earth has been discussed since the 1970s (e.g. Smylie & Mansinha 1971; Dahlen 1974; Chinnery 1975; Crossley & Gubbins 1975). It has been established that, subject to surface loading, the fluid core experiences perturbations in the potential, gravity and stress fields. The density perturbation is given by (e.g. Dahlen 1974; Tromp & Mitrovica 1999;

Martinec & Hagedoorn 2014)

$$\rho_1 = \frac{\partial_r \rho_0 (r)}{g_0 (r)} \phi_1 . \tag{2.4.1}$$

Following Zhong *et al.* (2003) and Latychev *et al.* (2005), we consider an incompressible core stratification satisfying the Williamson–Adams (WA) condition. For an incompressible sphere, this condition means a homogenous core which is always in a state of neutral equilibrium (Dahlen 1974). Inspection of eq. (2.4.1) shows that the density perturbation vanishes because there is no density stratification due to our assumption. This means that the core has no volumetric contribution to the perturbed potential field. Even if a stratified fluid core is assumed, the relative difference in viscoelastic responses to that of a fluid core without density perturbation is rather small ($\sim 5 \times 10^{-3}$; Martinec & Hagedoorn 2014). For models with a solution domain restricted in the mantle and lithosphere, the role of the fluid core reduces to the boundary conditions at the CMB where solutions from the mantle must match those from the core. In particular, a potential stress induced by the potential perturbation in the core needs to be considered at the CMB (see eq. 2.3.3). In Section 6, we particularly investigate the role of the potential stress on surface displacement and geoid.

2.5. The degree 1 deformation

Following Paulson *et al.* (2005), Geruo *et al.* (2013) and Blank *et al*. (2021), we also derive the displacement field in the Earth-load reference system (CM frame) with the origin at the instantaneous COM. ABAQUS calculates displacements in a coordinate system with the origin fixed at the centre of the initially undeformed spherical Earth, named the FE frame (Paulson *et al.* 2005). The displacement field in the FE frame differs from that in the CM frame by $\boldsymbol{d}_{\rm cm}$, a quantity identical to the translation of COM with respect to the FE frame. According to Martinec & Hagedoorn (2005), $\boldsymbol{d}_{\rm cm}$ can be calculated in the FE frame by

$$\boldsymbol{d}_{cm} (t) = \frac{1}{M} \left[\int_V \rho_0 (\boldsymbol{r}) \boldsymbol{u} (\boldsymbol{r}, t) \, {\rm d}V (\boldsymbol{r}) + \int_{\partial V} \sigma (\boldsymbol{r}, t) \boldsymbol{r} \, {\rm d}S (\boldsymbol{r}) \right] . \tag{2.5.1}$$

Here, M is the total mass of the Earth and load and $\boldsymbol{u}$ is the displacement field in the FE frame.

The first term in eq. (2.5.1) is the translation due to Earth's deformation. It can be further decomposed into the motion of the lithosphere and mantle (Klemann & Martinec 2011)

$$\boldsymbol{d}_S (t) = \frac{1}{M} \int_{V_S} \rho_0 (\boldsymbol{r}) \boldsymbol{u} (\boldsymbol{r}, t) \, {\rm d}V (\boldsymbol{r}) , \tag{2.5.2}$$

and the motion of the liquid core (Klemann & Martinec 2011)

$$\boldsymbol{d}_{lq} (t) = \frac{1}{M} \int_{\partial V_C} \rho_C (\boldsymbol{r}) u_r \boldsymbol{r} \, {\rm d}S (\boldsymbol{r}) . \tag{2.5.3}$$

The second term in eq. (2.5.1) is the translation due to surface loads, $\boldsymbol{d}_\sigma$, that is

$$\boldsymbol{d}_\sigma (t) = \frac{1}{M} \int_{\partial V} \sigma (\boldsymbol{r}, t) \boldsymbol{r} \, {\rm d}S (\boldsymbol{r}) . \tag{2.5.4}$$

Expanding $\boldsymbol{u}$ and σ into spherical harmonics, one can find that $\boldsymbol{d}_{\rm cm}$ is exclusively related to their degree-1 components. Subtracting $\boldsymbol{d}_{\rm cm}$ from $\boldsymbol{u}$, one can get the displacement field in the CM frame, that is $\boldsymbol{u}_{cm}$. Correspondingly, an additional mass of $-\Delta\rho \, \boldsymbol{d}_{\rm cm} \cdot \boldsymbol{e_r}$ is added to internal boundaries. Again, integrals in eqs (2.5.2)–(2.5.3) are evaluated with the two-point Gauss–Legendre quadrature rule directly in the spatial domain. Practically, we calculate $\boldsymbol{d}_{\rm cm}$ and $\boldsymbol{u}_{cm}$ as follows:

(1) Suppose the surface load at the current step i is σ_i, and the converged displacement field of the last step is $\boldsymbol{u}_{i-1}$ in the FE frame, then for the first iteration of the current step, $\boldsymbol{d}_{\rm cm}$ is calculated by inserting σ_i and $\boldsymbol{u}_{i-1}$ into eqs (2.5.2)–(2.5.4) while $\boldsymbol{u}_{\rm cm} = \boldsymbol{u}_{i-1} - \boldsymbol{d}_{\rm cm}$.

(2) After obtaining the displacement field of iteration 1 of the current step, $\boldsymbol{u}_i$, $\boldsymbol{d}_{\rm cm}$ is calculated by inserting σ_i and $\boldsymbol{u}_i$ into eqs (2.5.2)–(2.5.4) and $\boldsymbol{u}_{\rm cm} = \boldsymbol{u}_i - \boldsymbol{d}_{\rm cm}$;

(3) Repeat (2) for further iterations by calculating $\boldsymbol{d}_{\rm cm}$ and $\boldsymbol{u}_{\rm cm}$ of the current iteration with $\boldsymbol{u}_i$ from the last iteration, until $\boldsymbol{u}_i$ converges.

3 THE ITERATION SCHEME

Since we are following the IBF approach of Wong & Wu (2019), the iteration scheme here is similar to theirs. Suppose $\boldsymbol{u_{i-1}}$ and ϕ_{i-1} are displacement and potential solutions from the last iteration (or step) $i-1$, then the solution to displacement $\boldsymbol{u_i}$ of the current iteration (or step) i is obtained by solving the equilibrium equation

$$\nabla \cdot \boldsymbol{\tau} (\boldsymbol{u}_i) + \boldsymbol{b} (\boldsymbol{u}_{i-1}, \ \phi_{i-1}) = 0 \tag{3.1}$$

with ABAQUS, subject to surface loading pressure $P = \sigma_i \, g_0$ and potential pressure $P = -\rho_c \, \phi_{i-1}$ together with a Winkler foundation at the CMB. Here, $\boldsymbol{\tau}(\boldsymbol{u_i})$ and $\mathbf{b}(\boldsymbol{u_{i-1}}, \phi_{i-1})$ are the internal stress and body force at i, respectively. ϕ_i is then obtained by inserting $\boldsymbol{u_i}$ into eq. (2.2.9)

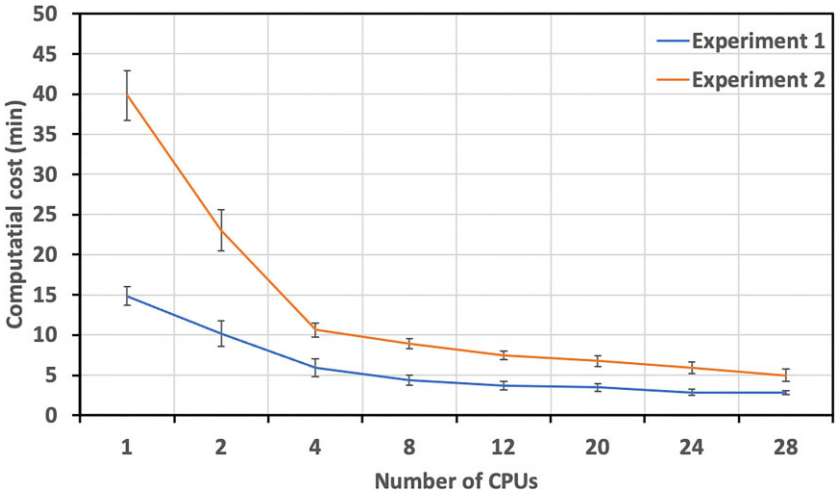

Figure 1. Two experiments showing how computation time changes with the number of CPUs in calculating the gravitational potential. Both experiments adopt the homogeneous compressible earth model 1a (Section 5.2) with Experiment 1 using a $2^\circ \times 1^\circ$ grid for depths $<$ 670km and a $4^\circ \times 2^\circ$ grid for depths $>$ 670km, and Experiment 2 using a uniform grid of $2^\circ \times 1^\circ$. Experiment 2 involves 833 040 3-D elements which is approximately twice of that of Experiment 1 (473 940). We did each experiment seven times; the mean computation time is treated as the y-axis value corresponding to each number of CPUs and the standard deviation is taken as the error bar value.

or (2.2.13). However, there are two differences from the iteration scheme in Wong & Wu (2019):

(1) In Wong & Wu (2019), when solving the equilibrium equation at the current step i, ABAQUS also needs to solve the equation for previous steps 1, 2, . . . , $i-1$. Here, by making use of the restart function, ABAQUS stores solutions at previous steps 1, 2, . . . , $i-1$ and only focuses on solving the equilibrium equation at i. With this improvement, the iteration scheme is $\sim$5 times faster than that of Wong & Wu (2019);

(2) As stated in Section 2.5, to view the displacement field in the CM frame, we subtract the translation of COM from the displacement calculated by ABAQUS. With this treatment, we find the displacement solution converges with up to 2 iterations less.

The reader is referred to Wong & Wu (2019) for more details about the iteration scheme.

4 COMPUTATIONAL EFFICIENCY OF FEMIBSF

The proposed computational scheme here is associated with solving the equation of equilibrium with commercial FE packages and solving Poisson's equation with codes written by us. The computation efficiency for the former is fully controlled by commercial FE packages; we cannot change the commercial codes to change the computation scheme, and thus, we do not discuss it in detail here. However, we note that ABAQUS is equipped with parallel computation which can be implemented on a single node with multiple cores. Thus, more CPUs provide faster calculations, which we observed in practice. On the other hand, as mentioned in Section 2.2, we also implemented parallel computation with OpenMP commands in solving Poisson's equation. To demonstrate its efficiency, we did two experiments with different grid resolutions for a homogeneous compressible earth model 1a (Section 5.2): the first experiment uses a $4^\circ \times 2^\circ$ grid for depths $>$670 km and a $2^\circ \times 1^\circ$ grid for depths $<$670 km, and the second uses a uniform grid of $2^\circ \times 1^\circ$ with the number of 3-D elements (833 040) being approximately twice of that of Experiment 1 (473 940). The computation cost versus the number of CPUs on a Linux machine for the two experiments is shown in Fig. 1: for both experiments the computation time indeed decreases with the increasing number of CPUs, implying a successful implementation of parallel computation of the gravitational potential. In addition, we note that the computation cost decreases in proportion (from 40 to $\sim$10 min for Experiment 1 and from 15 to $\sim$5 min for Experiment 2) to the number of CPUs increasing from 1 to 4 but does not decrease proportionally (and in fact by a much less extent) when CPUs increases from 4 to 28. The latter relatively low efficiency is caused by increased and less efficient interprocessor communication among the CPUs as well as the fact that more CPUs requires more time spent on creation of private variables, memory and computation task assignment. The minimum amount of time for a whole solution (Abaqus and Poisson equation solutions) cycle is achieved with 28 CPUs at $\sim$90 and 171 min for experiments 1 and 2, respectively.

5 VALIDATION

To validate our code/algorithm, we compare solutions generated with FEMIBSF with analytical solutions (Wu & Peltier 1982) for homogeneous models, and with numerical solutions from other established software for a layered model. In the following, we will first introduce these software, and then show comparison results.

Table 1. Material properties for the homogeneous compressible (1a), homogeneous incompressible (1b) and layered compressible (2a) models.

Layer	Lower radius (km)	Upper radius (km)	Density, ρ (kg m^{-3})	Young's modulus, E (Pa)	Poisson's ratio, ν	Viscosity, η (Pa·s)	Shear modulus, μ (Pa)	The second Láme parameter, λ (Pa)
				1a				
1	0.00	6371.00	5517	3.9325E + 11	0.3542	1.00E + 21	1.4519E + 11	3.5288E + 11
				1b				
1	0.00	6371.00	5517	4.3556E + 11	0.5000	1.00E + 21	1.4519E + 11	3.5288E + 15
				2a				
1	0.00	3485.5	10 977	Inviscid core, not modelled but boundary condition at the CMB considered				
2	3485.5	5200.0	5074	6.2410E + 11	0.2925	3.20E + 21	2.4143E + 11	3.4033E + 11
3	5200.0	5701.0	4527	4.5980E + 11	0.2730	1.60E + 21	1.8060E + 11	2.1719E + 11
4	5701.0	5971.0	3882	2.8300E + 11	0.2920	5.00E + 20	1.0952E + 11	1.5375E + 11
5	5971.0	6256.0	3442	1.8870E + 11	0.2901	5.00E + 20	7.3134E + 10	1.0108E + 11
6	6256.0	6371.0	3192	1.5470E + 11	0.2845	1.00E + 22	6.0218E + 10	7.9499E + 10

5.1 Software used for comparison

5.1.1 IBF

It is a Fortran 90 code written by Michael ChingKit Wong. The code is based on the IBF approach which represents all body forces in each finite element by their volumetric mean and solves the equilibrium equation iteratively with ABAQUS. The IBF code/algorithm is suitable for computing the viscoelastic responses of 1-D layered incompressible or compressible Earth models subject to spherical harmonic loading. Its validity has been verified by comparing the Love number results with those obtained with the NMM and the IST method (Wu 2004). More details of IBF can be found in Wong & Wu (2019).

5.1.2 ***ICEAGE***

This software uses Fortran and was developed by Georg Kaufmann. It applies the viscoelastic normal-mode method, thus can be used for spherically symmetric, radially varying (1-D) earth models (Kaufmann 2004). Kaufmann & Lambeck (2000; 2002) describe the theory implemented in ICEAGE in more details. The software can be used for incompressible but also compressible calculations. Latest modelling results were presented, for example, in Kierulf *et al.* (2021) and Reusen *et al.* (2023). Selected results that can be used for benchmarking are available since 1997 at http://rses.anu.edu.au/geodynamics/GIA_benchmark/index.html.

5.1.3 ***VILMA-C***

This Fortran code was developed by Yoshiyuki Tanaka and Volker Klemann. It is based on the spectral-finite element method (hereafter SFEM) proposed by Martinec (2000) of computing the viscoelastic relaxation of a spherical Earth with 3-D viscous structure. The SFEM has been extended to include compressibility (Tanaka *et al.* 2011), 3-D elasticity (Tanaka *et al.* 2009) as well as 3-D anelasticity (Huang *et al.* 2021). The elastic deformation for a homogeneous compressible earth model computed by VILMA-C fits to that computed by the Peltier-Wu formulism (Wu & Peltier 1982), while the viscoelastic deformation for 1-D stratified compressible earth models calculated by VILMA-C has been verified by a numerical Laplace integration method (Tanaka *et al.* 2009).

5.2 Homogeneous models

We first validate our results for incompressible and compressible homogeneous models, where density, elastic parameters and viscosity are all constants. This is vitally important because for homogeneous models, there are exact analytical elastic solutions (Wu & Peltier 1982), which numerical solutions must match reasonably well. For incompressible homogeneous models, exact analytical solutions also exist in the isostatic limit (Wu & Peltier 1982; Hanyk *et al.* 1999; Spada *et al.* 2011). But models with compressible layers and constant density result in long-term unstable behavior (Plag & Jüttner 1995; Hanyk *et al.* 1999; Vermeersen & Mitrovica 2000; Klemann *et al.* 2003). In Table 1, we show the density, Young's modulus, and Poisson's ratio values for compressible model 1a and incompressible model 1b. Table 2a shows the resolution and total number of nodes and 3-D elements used for 1a and 1b.

5.2.1 Variations of modelled surface displacement and gravitational potential with latitude

We start with looking at how FEMIBSF-computed surface displacement and gravitational potential vary with latitude. Since we apply a single harmonic load, $\sigma P_n(\theta)$ (where $P_n(\theta)$ is the Legendre function and θ the colatitude), it is expected that the computed vertical displacement

Table 2a. The horizontal and vertical resolutions at different radii and the total number of nodes and elements for models 1a and 1b for different harmonic degrees (n). The grid size followed by the layering thickness (or thickness of the finite element) are shown for different layers indicated by the radius range.

		1a/1b			
	Degree (n)	1	2	5	15
Radius (km)	0.0000−3480.0	2° × 4°,	485.7 km/2° × 4°,		485.7 km
	3480.0−5100.0	2° × 4°,	405.0 km/2° × 4°,		405.0 km
	5100.0−5701.0	2° × 4°,	150.25 km/2° × 4°,		200.3 km
	5701.0−5971.0	1° × 2°,	90.0 km/2° × 4°,		90.0 km
	5971.0−6271.0	1° × 2°,	60.0 km/2° × 4°,		150.0 km
	6271.0−6311.0	1° × 2°,	40.0 km/2° × 4°,		40.0 km
	6311.0−6371.0	1° × 2°,	30.0 km/2° × 4°,		30.0 km
Number of elements			473 940/178 200		
Number of nodes			509 490/188 370		

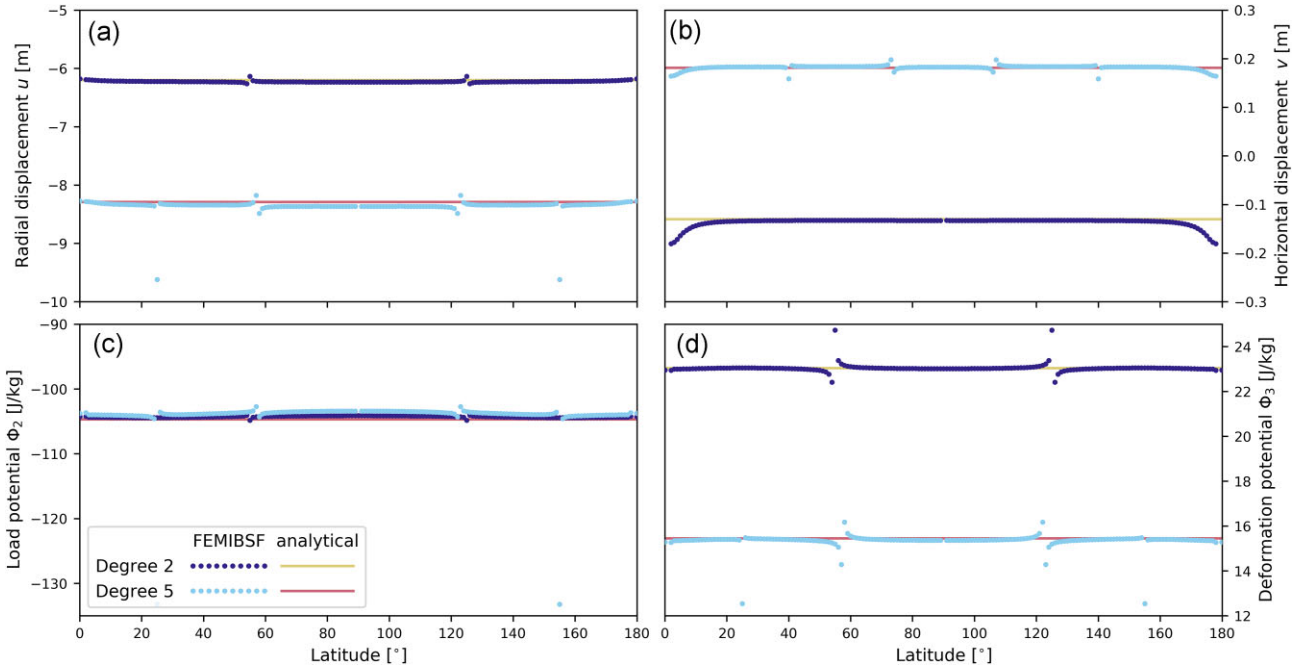

Figure 2. The spatial variation of ratios of displacement/potential with respect to Legendre function for the compressible model 1a for (a) radial displacement (u), (b) horizontal displacement (v), (c) load-induced potential (Φ_2) and (d) deformation potential (Φ_3). Shown here are results at the elastic limit. Blue dots are for FEMIBSF results and orange and red lines for analytical results. Note that the y-axis values refer to the ratios.

(u), horizontal displacement (v), load potential (ϕ_2) and deformation potential (ϕ_3) are proportional to the excitation, meaning the ratios, $u(\theta)/P_n(\theta)$, $v(\theta)/[\partial_\theta P_n(\theta)]$ [where $\partial_\theta P_n(\theta)$ is the first-order derivative of $P_n(\theta)$], $\phi_2(\theta)/P_n(\theta)$ and $\phi_3(\theta)/P_n(\theta)$, have to be constant. Fig. 2 shows the variation of these ratios for degrees 2 and 5 for model 1a at the elastic limit, with lines indicating analytical values calculated with the Peltier–Wu formalism (Wu & Peltier 1982; Tromp & Mitrovica 1999) and dots denoting our numerical solutions. It can be observed that for both displacement and potential, the calculated ratios are almost constant. Only at latitudes close to the roots of P_n or $\partial_\theta P_n(\theta)$ do deviations appear. For the horizontal displacement, however, the ratios deviate from a constant also near the polar latitudes. In the following, we investigate the reason behind this phenomenon.

We note that at the radius 5701 km, that is depth 670 km (the boundary between the lower and upper mantle), two different regular latitude-longitude grids, 1° × 2° and 2° × 4° are used for the upper and lower mantle, respectively (Table 2a). This non-conformal mesh has the advantage of accommodating less nodes in the lower mantle (so increasing computation speed) but also creates additional nodes that are used in the upper mantle but not in the lower mantle, that is the so-called hanging nodes (e.g. Fries *et al.* 2011). To see if the hanging nodes are related to horizontal displacement deviations near polar areas, we did three experiments with conformal meshes of different sizes (where the hanging nodes disappear): experiments 1 has a resolution of 2° × 4° which is lower than the non-conformal mesh resolution, while experiments 2 and 3 have resolutions of 1° × 2° and 1° × 1°, respectively, which are higher than the non-conformal mesh resolution. It can be seen that although a lower resolution is applied in experiment 1, the horizontal displacement deviations towards the polar area are greatly reduced compared to solutions based on the non-conformal mesh resolution (Fig. 3). Similarly, conformal meshes applied in experiments 2 and 3 are beneficial in reducing the deviations, with higher resolutions leading to smaller deviations and the deviations being less than 0.01

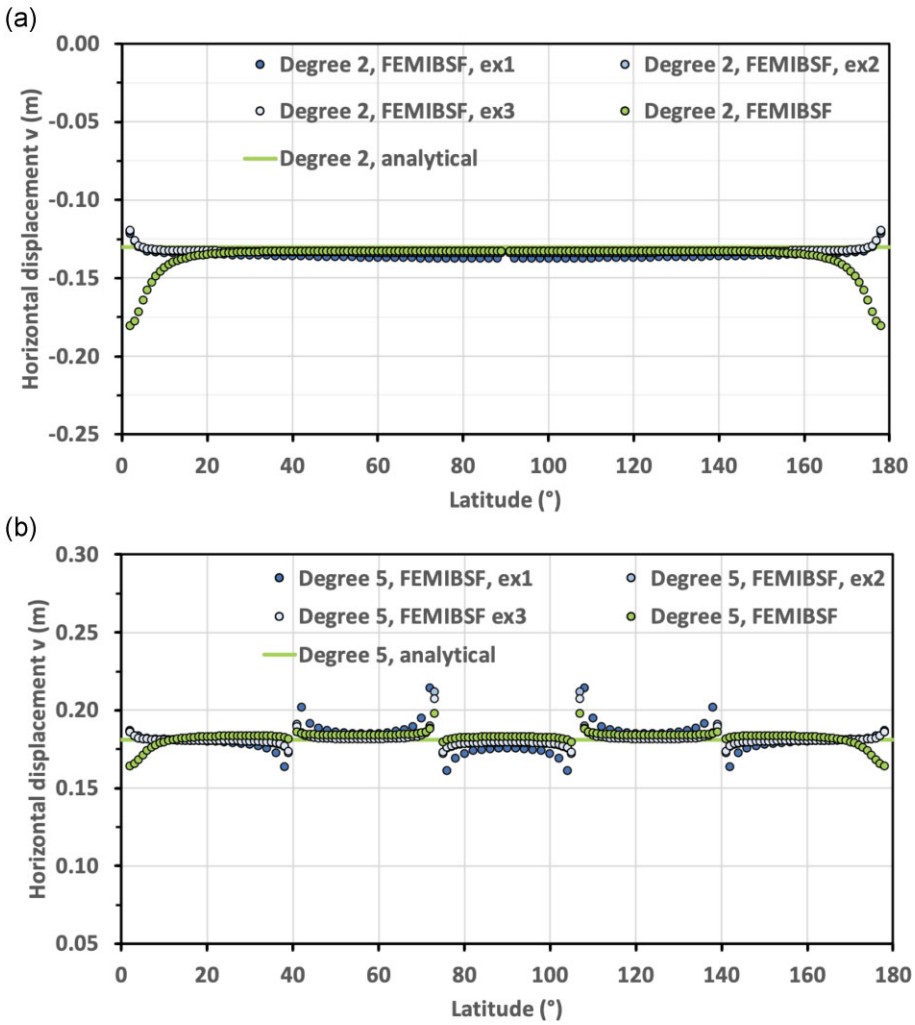

Figure 3. The variation of $v(\theta)/[\partial_\theta P_n(\theta)]$ of (a) degree 2 and (b) degree 5 for compressible model 1a for three experiments with conformal meshes of different regular grid sizes: experiment 1 (ex1) has a resolution of 2° × 4°, experiment 2 (ex2) has a resolution of 1° × 2°, and experiment 3 (ex3) a resolution of 1° × 1°. Also shown are the analytical solutions (Degree 2/5, analytical) and the numerical solutions (Degree 2/5, FEMIBSF) for a non-conformal mesh shown in Table 2a.

for both degrees 2 and 5 (Fig. 3). This level of deviations is acceptable given that the magnitude of horizontal displacements and that of $\partial_\theta P_n(\theta)$ become two orders and one order of magnitude smaller, respectively, when approaching the polar regions. Thus, we regard that hanging nodes, resolutions and numerical errors are the main causes of horizontal displacement deviations in polar areas.

5.2.2 Comparison of Love numbers

We now compare loading Love numbers (LLNs) h, l and k based on the FEMIBSF method with analytical solutions [again based on the PeltierWu formalism (Wu & Peltier 1982)] for models 1a and 1b in Table 3a. These LLNs are computed with the resolutions described in Table 2a. It is shown that, for degrees 1, 2 and 5, the differences in h, l and k between our solutions and the analytical solutions are in general less than 2 per cent in both the elastic and viscous limits (for incompressible model 1b). This can be regarded as a rather good match, considering the inevitable error caused by numerical integration and interpolation used in calculating displacement, potential and body force. For degree 15, the differences in LLNs increase for both compressible and incompressible models. For the compressible model 1a, the differences are not greater than 3.1 per cent, still a reasonably good match. For the incompressible model 1b, the difference in h is less than 3 per cent, but the differences are a bit larger (∼8 per cent) for l and k. We note that although hanging nodes exist at the lower-upper mantle boundary of model 1a (Table 2a), the errors in FEMIBSF-modelled Love numbers h, l and k up to degree 15 are less than 3 per cent, which can be regarded as a minor impact. In addition, Table 3a reveals that the higher the spherical harmonic degree, the larger the differences in h, l and k between analytical and finite-element solutions, which is consistent with Zhong *et al.* (2003) and Geruo *et al.* (2013). As they argued, resolving shorter wavelength (higher spherical harmonic degree) displacement and potential requires a higher FE resolution. This is a rather general comment on the difference between numerical and analytical solutions. In the following, we explore in detail the reason for the generation of the error.

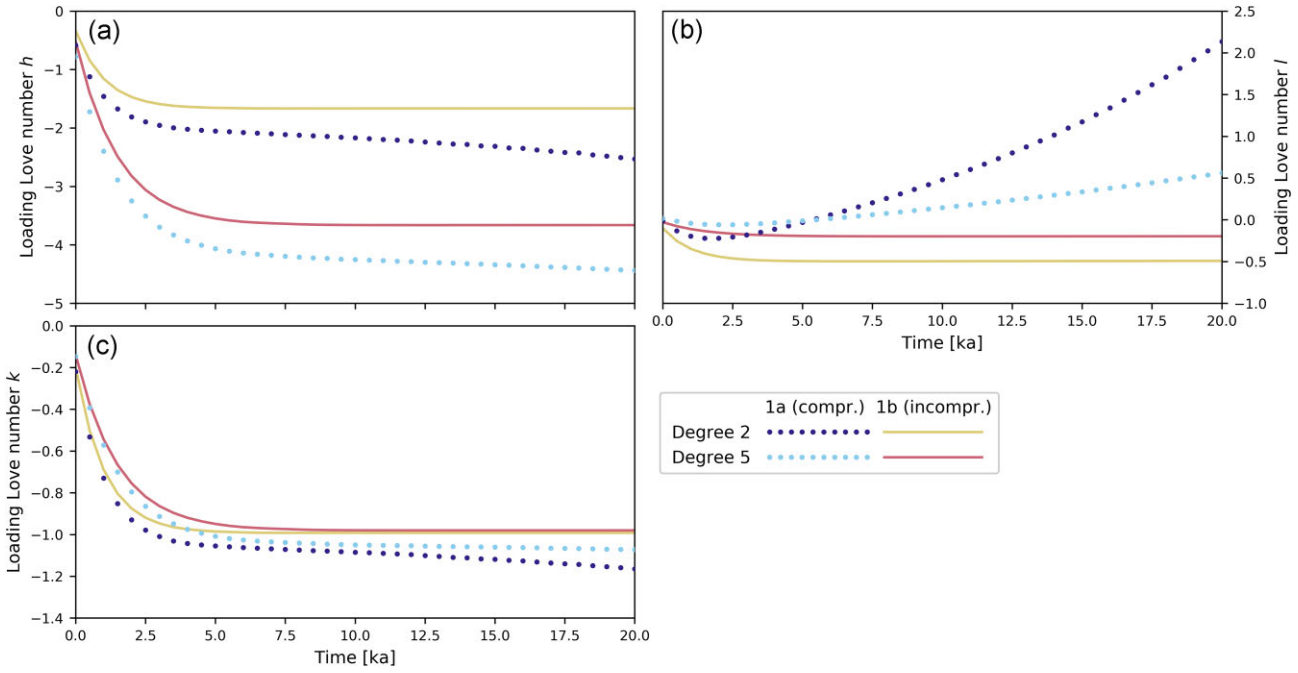

Figure 4. Comparison of the time evolution of loading Love numbers of degrees 2 and 5 for the compressible model 1a and the incompressible model 1b. Blue dots are for model 1a and lines for model 1b. The subplot A is for h, B is for l and C is for k.

Table 3b shows the difference between the modelled and analytical solutions of load potential ϕ_2, that is the driving potential of GIA. It can be seen that the absolute value of the modelled ϕ_2 (ϕ_2 is negative) is less than its analytical value; moreover, as the resolution is fixed for all degrees (Table 2a) the difference between modelled and analytical ϕ_2 increases with degree (n) because resolving shorter wavelength ϕ_2 requires higher resolution. As a consequence, the modelled deformation potential ϕ_3 (ϕ_3 is positive), that is the responding potential of GIA which scales with the modelled ϕ_2, is smaller than its analytical solution with the difference increasing with n as well (starting from $n = 2$; see Table 3a for *k_FEMIBSF* results). It can be inferred that the absolute value of modelled ϕ_1 (ϕ_1 is negative), that is the full potential of GIA being the sum of ϕ_2 and ϕ_3 but dominated by ϕ_2, is also smaller than its analytical value. Wong & Wu (2019) have shown that the surface pressure by the load and the self-gravity $-\nabla(\rho_0\phi_1)\cdot\boldsymbol{e_r}$ are the two dominant initial driving forces of Earth's deformation, with the latter acting against the former. Since $-\phi_1$ is smaller its analytical value in magnitude, $-\nabla(\rho_0\phi_1)\cdot\boldsymbol{e_r}$ is smaller than its analytical value as well. It follows that there should be a larger deformation than the theoretical one in the elastic limit. This is confirmed in Table 3a by larger $-h$ and $-l$ than their analytical values (degree 15 l for incompressible model 1b shown in Table 3a is an exception due to the insufficient horizontal resolution adopted, as will be demonstrated in Table 4a).

Note that, to reduce the numerical errors in deformation potential ϕ_3 as well as those in vertical and horizontal displacements, we can use the analytical solution to ϕ_2 in our calculations for harmonic loads. However, for realistic load distributions, analytical solutions to ϕ_2 do not exist. Since our theory and code is designed for realistic load simulations, we do not apply the analytical solutions here, but adopt the numerical integration method to calculate ϕ_2 and test how accurate this integration is under the given resolution. From Table 3a we can observe that under the current resolution, the errors in degree 15 Love numbers l and k for model 1b are largest, being much larger than 3 per cent. To reduce these relative larger errors and to further test the accuracy of our computation scheme, we did two more experiments with a degree 15 load for model 1b but using higher spatial resolutions, namely experiment 2 and 3 with resolutions of $2^\circ \times 2^\circ$ and $1^\circ \times 2^\circ$, respectively (we refer to experiment 1 as the one using the resolution from Table 2a, i.e. $2^\circ \times 4^\circ$). Not surprisingly, as the resolution increases, larger amount of mass density at Earth's surface gets sampled and so the modelled driving potential Φ_2 approaches its analytical value with the difference decreasing from 6.49 to 2.81 per cent (Table 4b) (it follows that the modelled driving force of GIA gets close to its theoretical value as well). As a consequence, the errors in modelled deformation potential Φ_3, and the horizontal displacement decrease significantly from being greater than 200 and 8 per cent (for Love numbers l and k, respectively) to being less than 1.5 and 3.5 per cent (Table 4a). Therefore, we demonstrate that increasing the resolution reduces the error in the modelled driving potential (as well as the driving force) of GIA, which leads to accuracy improvement in modelled displacement and deformation potential.

5.2.3 Unstable modes for compressible model 1a

The compressible model 1a adopted here is the same as the one considered in Hanyk *et al.* (1999) and Vermeersen & Mitrovica (2000). It has been shown that due to violation of the Williamson–Adams (WA) stability condition, model 1a is subject to the Rayleigh–Taylor (RT) instability. To see if FEMIBSF can reproduce the instability, we examine in Fig. 4 the evolution of LLNs with time for models 1a and 1b. It

Table 2b. Same as Table 2a but for model 2a.

			2a			
Degree (n)			1	2	5	15
Radius (km)	Lower mantle	3485.5−5200.0	2° × 4°,	81.5 km	2° × 4°, 285.5 km	1° × 1°, 285.5 km
		5200.0−5701.0	2° × 4°,	83.5 km	2° × 4°, 125.3 km	1° × 1°, 125.3 km
	Upper mantle	5701.0−5971.0	2° × 4°,	54.0 km	1° × 2°, 67.5 km	1° × 1°, 67.5 km
		5971.0−6256.0	2° × 4°,	57.0 km	1° × 2°, 57.0 km	1° × 1°, 57.0 km
	Lithosphere	6256.0−6371.0	2° × 4°,	28.8 km	1° × 2°, 28.8 km	1° × 1°, 28.8 km
Number of elements			332 100		497 520	1 473 840
Number of nodes			343 980		532 980	1 546 560

Table 3a. Loading Love numbers h, l and k comparison between finite element (FEMIBSF) and analytical (an) results for the homogeneous earth models 1a and 1b for degrees (n) 1, 2, 5 and 15 as well as their difference (error) in per cent. For model 1b, the degree 1, 2 and 5 values at the isostatic limit are the values at 20 ka (thousand years) after loading because we found that Love number values remain constant after ∼7.5 ka (see Fig. 4). The degree 15 value is the value at 25 ka. LLNs were calculated with the resolutions shown in Table 2a.

				1a, elastic limit					
n	*h_FEMIBSF*	*h_an*	Error (per cent)	*l_FEMIBSF*	*l_an*	Error (per cent)	*k_FEMIBSF*	*k_an*	Error (per cent)
1	−1.1828E + 00	−1.1827E + 00	0.01	−8.5775E-01	−8.5660E-01	0.13	−9.9815E-01	−1.0000E + 00	0.19
2	−5.8392E-01	−5.8167E-01	0.39	−1.2522E-02	−1.2200E-02	2.65	−2.1996E-01	−2.2009E-01	0.06
5	−7.8259E-01	−7.7766E-01	0.63	1.7091E-02	1.7002E-02	0.52	−1.4698E-01	−1.4761E-01	0.43
15	−9.3041E-01	−9.2332E-01	0.77	1.1810E-02	1.1454E-02	3.10	−6.4592E-02	−6.6333E-02	2.70
				1b, elastic limit					
n	*h_FEMIBSF*	*h_an*	Error (per cent)	*l_FEMIBSF*	*l_an*	Error (per cent)	*k_FEMIBSF*	*k_an*	Error (per cent)
1	−1.0002E + 00	−1.0001E + 00	0.01	−1.0000E + 00	−1.0001E + 00	0.01	−9.9516E-01	−1.0000E + 00	0.48
2	−3.3644E-01	−3.3360E-01	0.85	−1.0092E-01	−1.0008E-01	0.84	−2.0020E-01	−2.0016E-01	0.02
5	−5.1473E-01	−5.1345E-01	0.25	−2.8234E-02	−2.8006E-02	0.81	−1.3783E-01	−1.4003E-01	1.58
15	−6.5404E-01	−6.7162E-01	2.62	−3.9772E-03	−4.3331E-03	8.21	−5.9687E-02	−6.4996E-02	8.17
				1b, isostatic limit					
n	*h_FEMIBSF*	*h_an*	Error (per cent)	*l_FEMIBSF*	*l_an*	Error (per cent)	*k_FEMIBSF*	*k_an*	Error (per cent)
1	−1.0007E + 00	−1.0001E + 00	0.06	−9.8201E-01	−1.0001E + 00	1.81	−9.9502E-01	−1.0000E + 00	0.50
2	−1.6659E + 00	−1.6667E + 00	0.04	−4.9152E-01	−5.0000E-01	1.70	−9.9201E-01	−1.0000E + 00	0.80
5	−3.6614E + 00	−3.6667E + 00	0.14	−1.9691E-01	−2.0000E-01	1.55	−9.8020E-01	−1.0000E + 00	1.98
15	−1.0250E + 01	−1.0333E + 01	0.76	9.7500E-02	−6.6667E-02	246	−9.2260E-01	−1.0000E + 00	7.74

Table 3b. Comparison of load-induced potential Φ_2 (driving potential of GIA) for the homogeneous compressible and incompressible models 1a and 1b, respectively, between finite element (FEMIBSF) and analytical (an) results. Φ_2 is computed using the resolutions shown in Table 2a.

	1a			1b		
n	$\Phi_{2\_\mathrm{FEMIBSF}}$ (J/kg)	Φ_2_an (J/kg)	Error (per cent)	$\Phi_{2\_\mathrm{FEMIBSF}}$ (J kg^{-1})	Φ_2_an (J kg^{-1})	Error (per cent)
1	1.0445E + 02	1.0469E + 02	0.23	1.0419E + 02	1.0469E + 02	0.48
2	1.0429E + 02	1.0469E + 02	0.39	1.0385E + 02	1.0469E + 02	0.81
5	1.0378E + 02	1.0469E + 02	0.87	1.0275E + 02	1.0469E + 02	1.86
15	1.0175E + 02	1.0469E + 02	2.81	9.7894E + 01	1.0469E + 02	6.49

is evident that for the incompressible model 1b, the solutions to h, l and k are stable, all reaching the isostatic limit after ∼5 ka for degree 2 and ∼10 ka for degree 5. However, for compressible model 1a the solutions to h, l and k do not converge: unstable modes are apparent for h and k after ∼10 ka for degree 2 and after a longer timescale for degree 5, while the instability for l appears as early as ∼3 ka. The instability is associated with the strength and characteristic time scale of unstable modes. As pointed out by Hanyk *et al.* (1999) and Vermeersen & Mitrovica (2000), the characteristic time scale of the highest-strength unstable mode RT1 for vertical displacement and perturbed potential is ∼10 ka for degree 2 and increases with increasing spherical harmonic degrees; for the horizontal displacement, since the strengths of the unstable modes are much larger than that of the stable modes, the unstable modes can appear much earlier in the time evolution of Love number l. To sum up, it is shown here that FEMIBSF can directly reveal the unstable modes in the time domain, the existence of which is an important characteristic of compressible earth models.

5.3 The layered model

In this section, we verify our results for a six-layer compressible model 2a (see Table 1 for material properties and Tables 2b and 5a for the resolution) which has been considered in Wong & Wu (2019). This model has a similar viscosity profile to VM5a, a 1-D viscosity model frequently used in GIA modelling (Peltier *et al.* 2015). We apply single harmonic loads with a Heaviside history.

Table 4a. Degree 15 Love numbers comparison for model 1b between analytical solutions (*h_an*, *l_an* and *k_an*) and numerical solutions based on FEMIBSF (*h_FEMIBSF*, *l_FEMIBSF* and *k_FEMIBSF*) from three experiments. Experiments 1, 2 and 3 have increasing uniform grids of $2^\circ \times 4^\circ$, $2^\circ \times 2^\circ$ and $1^\circ \times 2^\circ$, respectively.

				Elastic limit					
Experiment	*h_FEMIBSF*	*h_an*	Error (per cent)	*l_FEMIBSF*	*l_an*	Error (per cent)	*k_FEMIBSF*	*k_an*	Error (per cent)
1	6.5404E-01	6.7162E-01	2.62	−3.9772E-03	−4.3331E-03	8.21	−5.9687E-02	−6.4996E-02	8.17
2	6.5620E-01	−6.7162E-01	2.30	−4.500E-03	−4.3331E-03	3.85	−5.9900E-02	−6.4996E-02	7.84
3	6.6820E-01	−6.7162E-01	0.51	−4.400E-03	−4.3331E-03	1.54	−6.2700E-02	−6.4996E-02	3.53
				Isostatic limit					
Experiment	*h_FEMIBSF*	*h_an*	Error (per cent)	*l_FEMIBSF*	*l_an*	Error (per cent)	*k_FEMIBSF*	*k_an*	Error (per cent)
1	−1.0250E + 01	−1.0333E + 01	0.76	9.7500E-02	−6.6667E-02	246	−9.2260E-01	−1.0000E + 00	7.74
2	−1.0282E + 01	−1.0333E + 01	0.49	−7.4900E-02	−6.6667E-02	12.35	−9.3440E-01	−1.0000E + 00	6.56
3	−1.0329E + 01	−1.0333E + 01	0.04	−6.7600E-02	−6.6667E-02	1.40	−9.6790E-01	−1.0000E + 00	3.21

Table 4b. Same as 4a but for the Load-induced potential Φ_2 (driving potential of GIA).

Experiment	$\Phi_{2\_FEMIBSF}$ ($J\,kg^{-1}$)	Φ_{2}_an ($J\,kg^{-1}$)	Error (per cent)
1	−9.7894E + 2	−1.0469E + 02	6.49
2	−9.9211E + 2	−1.0469E + 02	5.23
3	−10.175E + 2	−1.0469E + 02	2.81

Table 5a. The horizontal resolutions used for model 2a in five experiments with FEMIBSF for a degree 15 spherical harmonic load. The vertical resolution is fixed for the five experiments and the same as that shown in Table 2b for degree 15.

Experiment			1	2	3	4	5
Radius (km)	Lower mantle	3485.5−5200.0	$2^\circ \times 4^\circ$	$1^\circ \times 2^\circ$	$1^\circ \times 1^\circ$	$2^\circ \times 4^\circ$	$2^\circ \times 4^\circ$
		5200.0−5701.0	$2^\circ \times 4^\circ$	$1^\circ \times 2^\circ$	$1^\circ \times 1^\circ$	$2^\circ \times 4^\circ$	$2^\circ \times 4^\circ$
	Upper mantle	5701.0−5971.0	$2^\circ \times 4^\circ$	$1^\circ \times 2^\circ$	$1^\circ \times 1^\circ$	$1^\circ \times 2^\circ$	$1^\circ \times 2^\circ$
		5971.0−6256.0	$2^\circ \times 4^\circ$	$1^\circ \times 2^\circ$	$1^\circ \times 1^\circ$	$1^\circ \times 2^\circ$	$1^\circ \times 2^\circ$
	Lithosphere	6256.0−6371.0	$2^\circ \times 4^\circ$	$1^\circ \times 2^\circ$	$1^\circ \times 1^\circ$	$1^\circ \times 2^\circ$	$0.5^\circ \times 1^\circ$

5.3.1 Love numbers comparison

It has been shown that for model 2a, the unstable modes are pronounced only after more than a hundred thousand years of loading, that is the timescale of one glacial–interglacial cycle (Wong & Wu 2019). To reduce computational efforts, our calculations are restricted to the first 40 ka. We compare our results with numerical solutions from VILMA-C in Fig. 5 (see the caption of Fig. 5 for resolutions used in the Love number computations). Inspection of Fig. 5 shows that our solutions (dotted line) match those from VILMA-C (solid line) rather well for *h, l* and *k* of degrees 1, 2 and 5, with the relative differences between FEMIBSF and VILMA-C being less than 0.8 per cent for *h*, less than 2.5 per cent for *l* and less than 0.8 per cent for *k*. For degree 15, results for *h* agree quite well between FEMIBSF and VILMA-C with the relative differences being less than 1.3 per cent, while the differences for *l* and *k* are larger than 3.0 per cent. The particularly large relative difference for *l* is due to its small absolute magnitude, being two orders of magnitude smaller than that of *h* and close to 0 at ∼2 ka (Figs 5 and 6). The large differences for *l* and *k*, as we will see below, are associated with resolution.

To investigate the influence of resolution for the layered compressible model 2a on degree 15 Love numbers, we did three experiments using FEMIBSF with increasing uniform regular grid resolutions (see Table 5a for resolutions used in experiments 1, 2 and 3) and three experiments using VILMA-C with increasing uniform Gaussian–Legendre grid resolutions (see Table 5b for resolutions). Note that, to minimize the impact of vertical resolution, VILMA-C uses much finer vertical resolution than FEMIBSF. The obtained Love number results for these experiments are shown in Fig. 6. It can be observed that for VILMA-C, increasing the horizontal (compare resolutions of experiments 1 and 2) or vertical (compare resolutions of experiments 2 and 3) resolution changes the modelled degree 15 Love numbers *h*, *l* and *k* minorly (by less than 0.5 per cent) which implies that Love number solutions calculated with VILMA-C reach convergence. Thus, we treat solutions by VILMA-C as the standard solutions, and deviations from these solutions as errors. On the other hand, as expected, increasing the resolution reduces the differences in modelled Love numbers (for *l* and *k* in particular) between FEMIBSF and VILMA-C, and when the resolution reaches that of Experiment 3 for FEMIBSF, that is $1^\circ \times 1^\circ$, the Love number curves of FEMIBSF and VILMA-C become rather close for *h* and *l* (compare FEMIBSF and VILMA-C curves for experiments 1, 2 and 3 in Figs. 6a, 6b and 6c). The reason is that with increasing resolution, the driving potential ϕ_2 calculated with FEMIBSF gets closer to its theoretical value (Fig. 6d), which leads to the modelled driving force of GIA being closer to its theoretical value. In addition, we note that in the case of Experiment 3 with FEMIBSF, the difference in Love number *k* between FEMIBSF and VILMA-C is as large as 4.5 per cent, which means a higher resolution is still needed. But, we also observed that for FEMIBSF, if the modelled responding potential of GIA, that is ϕ_3, (which is theoretically in proportion to the modelled ϕ_2) is divided by the modelled driving potential ϕ_2 (instead of the theoretical ϕ_2), then the obtained Love number *k* values fit perfectly those of VILMA-C (see Figs 5 and 6 for the *k* Love number results labelled as 'Degree 15, FEMIBSF, ex3, M'). The resulting differences are less than 1 per cent

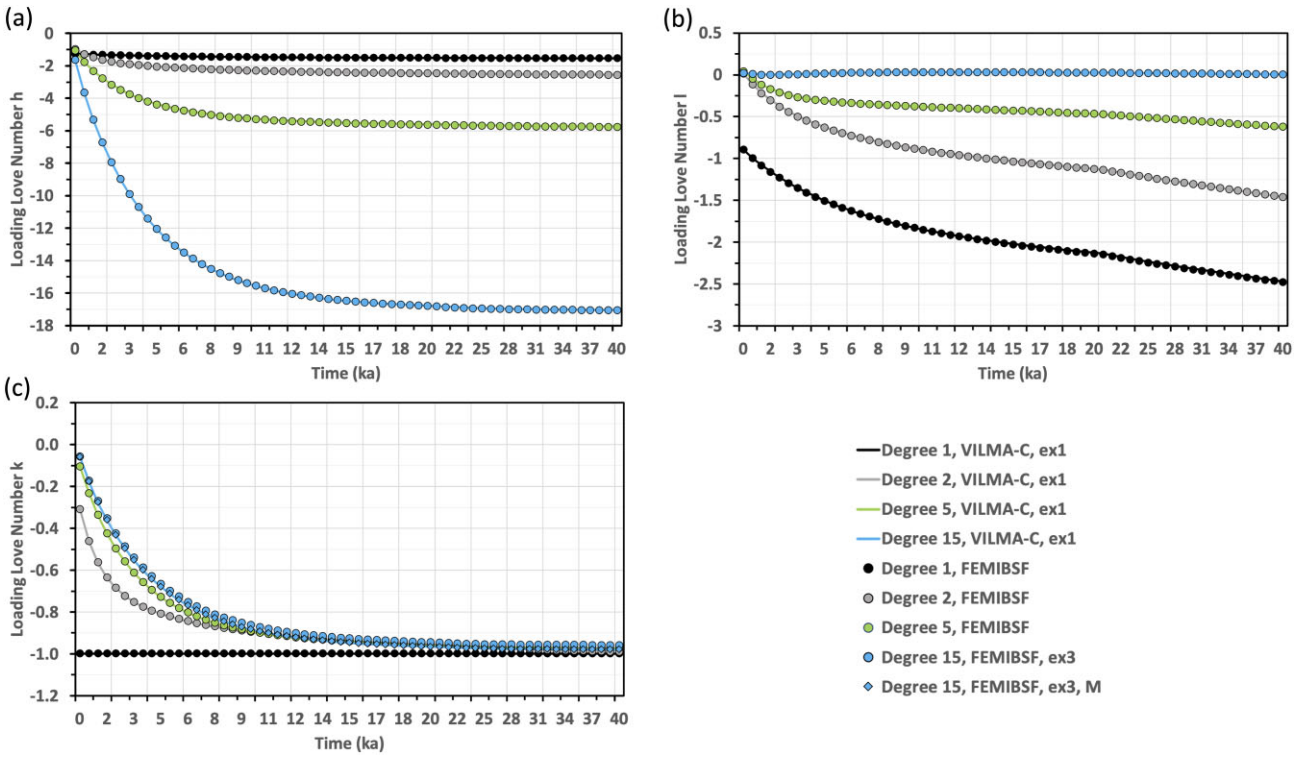

Figure 5. Loading Love numbers (h, l and k) comparison between VILMA-C and FEMIBSF for the compressible model 2a. FEMIBSF Love numbers are computed using the resolution shown in Table 2b while VILMA-C results are obtained with the resolution shown in Table 5b. The Love number k results labelled as 'Degree 15, FEMIBSF, ex3, M' is obtained by dividing the ϕ_3 values by the modelled value of ϕ_2 instead of its theoretical value (see Fig. 6d for the difference between theoretical ϕ_2 and modelled ϕ_2 by FEMIBSF). Note that, it is the modelled value of ϕ_2 that drives GIA in our modelling. ex1 and ex3 refer to experiments 1 and 3, respectively. See Table 5 for the resolutions used in each experiment.

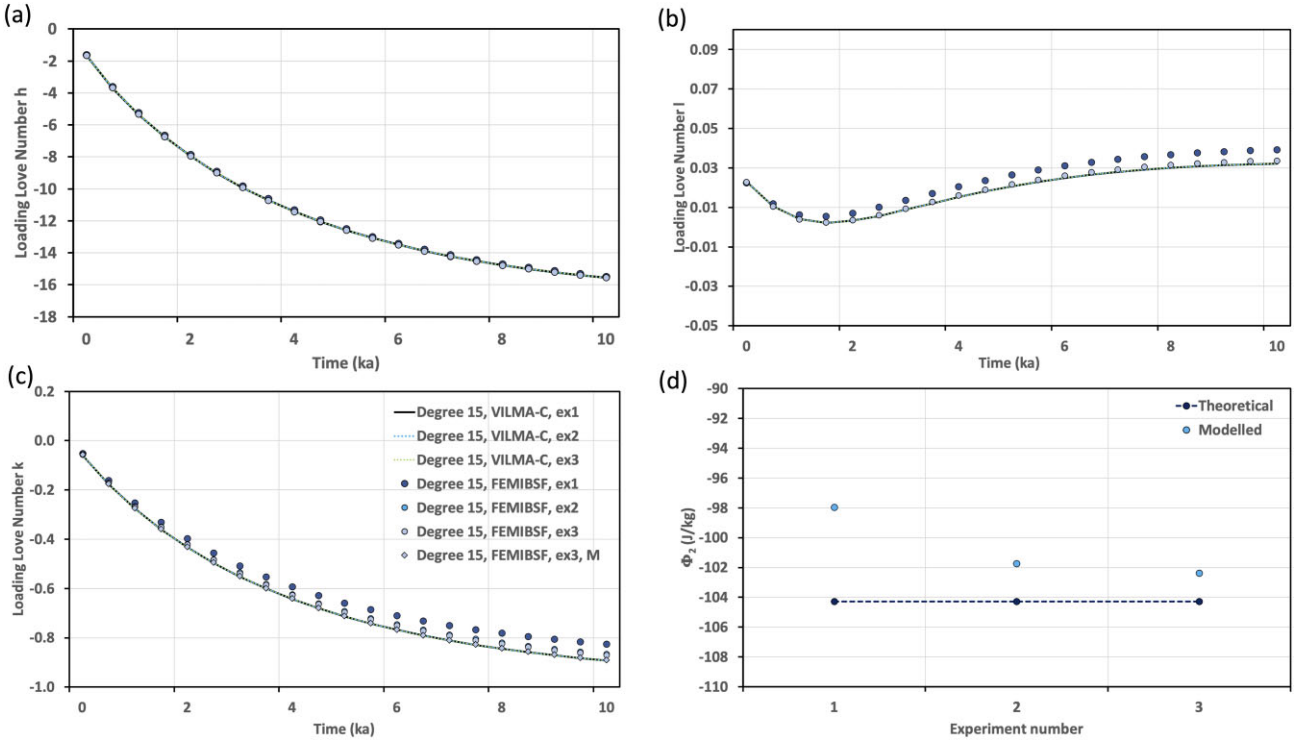

Figure 6. Resolution experiments for model 2a Love numbers and load potential Φ_2 of degree 15. Three tests, ex1, ex2 and ex3 referring to experiments 1, 2 and 3, respectively, were performed for FEMIBSF and VILMA-C. The Love number k curve labelled 'Degree 15, FEMIBSF, ex3, M' is the same as that in Fig. 5. See Table 5a and Table 5b for the resolution of each experiment used by FEMIBSF and VILMA-C, respectively.

Table 5b. The resolutions used for model 2a in three experiments with VILMA-C for spherical harmonic load of degree 15 (as well as degrees 1, 2 and 5).

Experiment			1	2	3
Radius (km)	Lower mantle	3485.5−5200.0	40 km	40 km	40 km
		5200.0−5701.0	40 km	40 km	40 km
	Upper mantle	5701.0−5971.0	10 km	10 km	10 km
		5971.0−6256.0	5 km	5 km	5 km
	Lithosphere	6256.0−6371.0	5 km	5 km	2 km
Number of Gaussian–Legendre grids for each layer			98 × 256	386 × 1024	386 × 1024

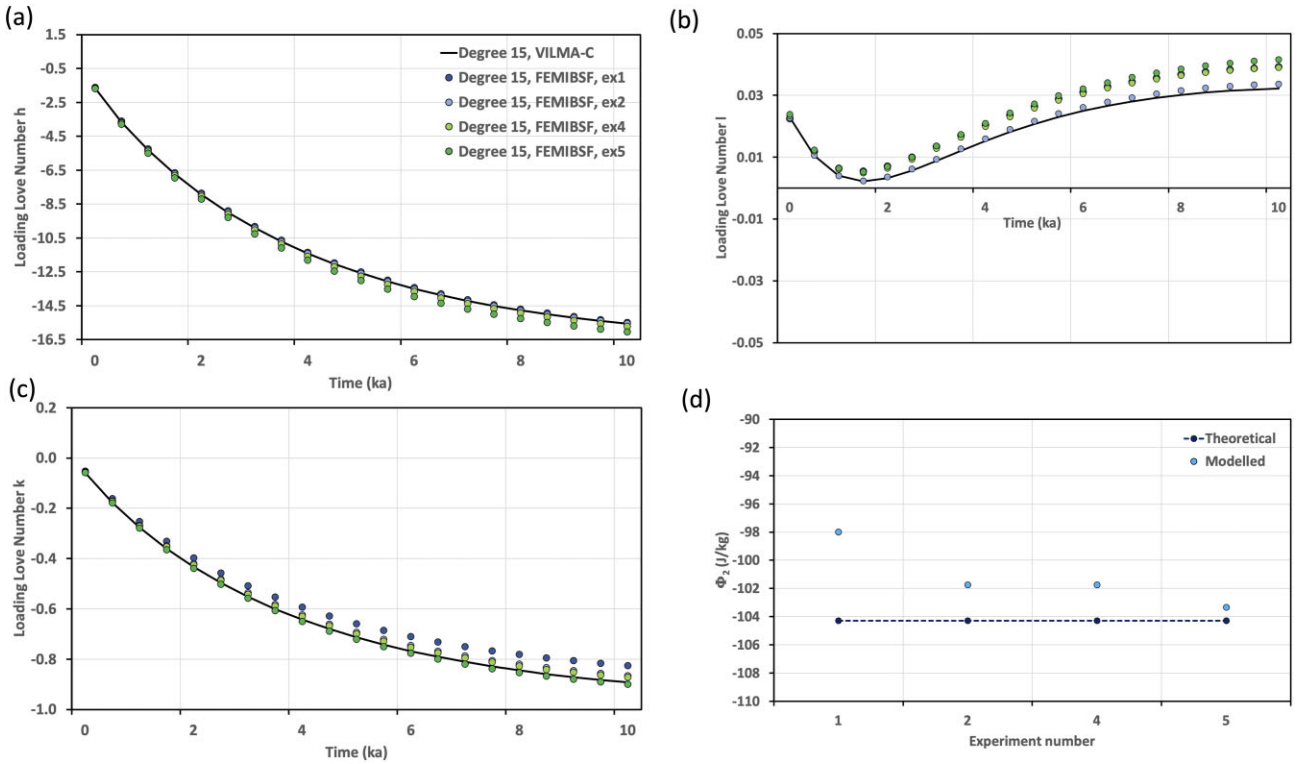

Figure 7. Comparison of degree 15 LLNs of model 2a for experiments with different conformal and non-conformal meshes. See Table 5 for the specification of each experiment.

(except the one at the elastic limit when the absolute k value is as small as -0.06). This is reasonable because it is the modelled value of ϕ_2 that drives GIA instead of its theoretical value. To sum up, increasing spatial resolution leads to improvement in modelled displacement and potential by FEMIBSF for a layered compressible model in addition to homogeneous models.

5.3.2 Consequences of hanging nodes for modelled displacement and potential

In section 5.2, we showed that hanging nodes at the lower-upper mantle boundary of the homogeneous compressible earth model 1a have a minor impact on Love numbers h, l and k up to degree 15 at the elastic limit but lead to relatively large errors in modelled horizontal displacement towards polar latitudes. Here, we further investigate the consequence of hanging nodes within the layered compressible model 2a for degree 15 Love numbers not only at the elastic limit but also in the viscous regime (up to 10 ka). Two more experiments, that is experiments 4 and 5, using non-conformal grids have been done with FEMIBSF to achieve this purpose: compared to experiment 1 (using a conformal grid of $2^\circ \times 4^\circ$), experiment 4 has a higher resolution of $1^\circ \times 2^\circ$ in the upper mantle and lithosphere, and so hanging nodes exist at the lower-upper mantle boundary (depth 670 km, see Table 5a), while experiment 5 has higher resolutions of $1^\circ \times 2^\circ$ and $0.5^\circ \times 1^\circ$ in the upper mantle and lithosphere, respectively, and so hanging nodes exist at both the lower-upper mantle boundary and the mantle-lithosphere boundary (depth 115 km, see Table 5a).

Fig. 7 shows the Love number solutions by FEMIBSF from the aforementioned experiments and the converged solutions by VILMA-C which act as the standard solutions. Compared to FEMIBSF experiment 1, higher resolutions in the upper mantle and lithosphere in experiments 4 and 5 lead to more accurate solutions to Love number k and Φ_2 (Figs 7c and d), not surprising because more mass density gets sampled, but poorer solutions to Love numbers h and l, especially in the viscous regime (Figs 6a and b). The latter can be traced back to the hanging nodes at the lower-upper mantle boundary in both experiments 4 and 5, as well as the mantle-lithosphere boundary in

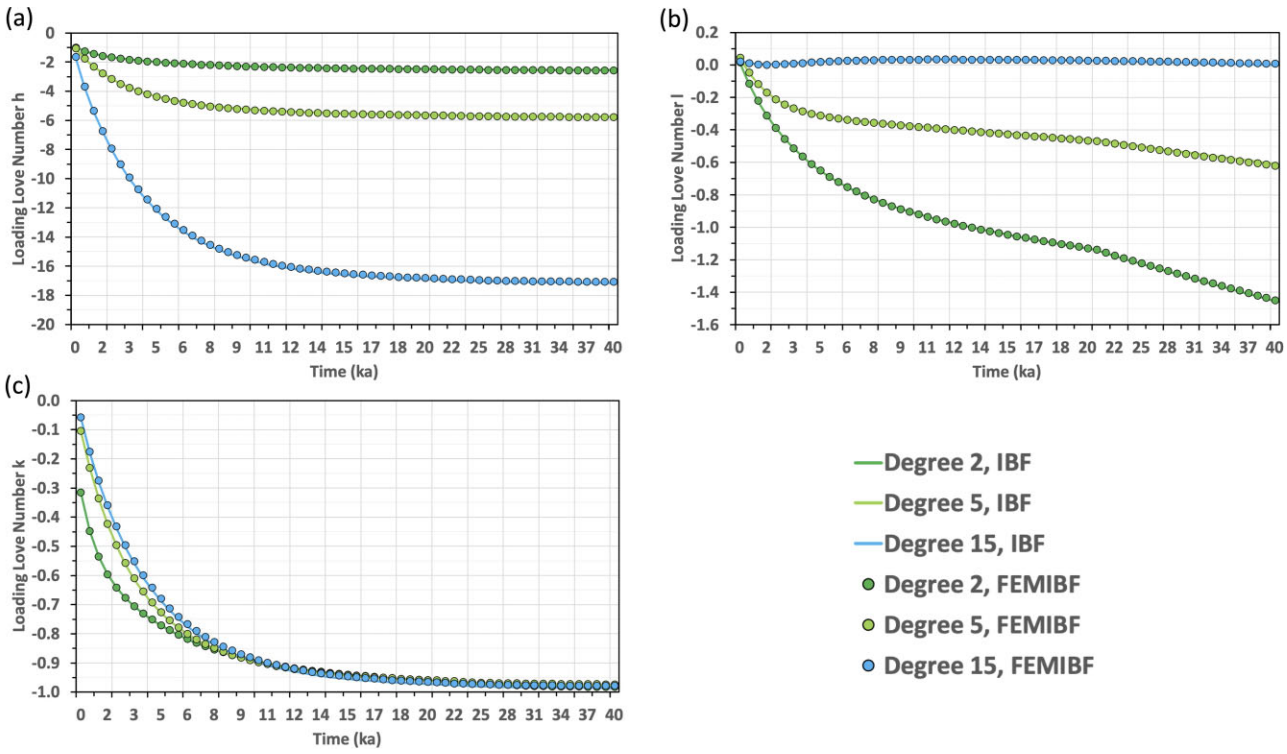

Figure 8. Comparison of Love number solutions by IBF and FEMIBF (the version of FEMIBSF without considering the potential stress at the CMB).

experiment 5. In particular, hanging nodes at the mantle–lithosphere boundary (experiment 5) lead to even poorer solutions to horizontal and vertical displacement (Figs 7a and b). In contrast, if a conformal mesh with a higher resolution than that of experiment 1 is adopted without creating hanging nodes, for example the $1^\circ \times 2^\circ$ resolution in experiment 2, the numerical solutions are not only improved for the driving and responding potential but also for the vertical and horizontal displacements (Fig. 7).

6 APPLICATIONS

6.1 The effect of potential stress at CMB on displacement and gravitational potential at Earth's surface

The impact of a fluid core on static deformation and the gravitational potential of the mantle and lithosphere can be modelled by considering the effects of the buoyancy force and potential stress at the CMB (Section 2.4). The essential point is whether this impact can be revealed at the surface of the Earth, which might be detected/confirmed by modern space geodetic techniques such as GNSS and GRACE. Thus, in this section we examine the role of the potential stress in shaping surface displacement and gravitational potential (geoid) through modelling.

Fig. 8 compares the Love numbers between FEMIBF (the version of FEMIBSF without considering the potential stress) and IBF (Wong & Wu 2019). It can be seen that the solutions obtained from IBF which also do not take into account potential stress are well matched by the FEMIBF solutions with relative differences generally less than 1 per cent. This confirms the validity of the FEMIBF solutions. Furthermore, the differences between FEMIBSF and FEMIBF solutions (shown in Fig. 9) indicate that potential stress at the CMB has a considerable effect on degree 2 Love numbers (with differences as large as 0.08, 0.03 and 0.05 for h, l and k, respectively), a minor effect on degree 5 Love numbers (differences up to 0.01 for h, l and k) and virtually no impact on degree 15 Love numbers. This is reasonable as the wavelength of degree 2 displacement and potential penetrates much deeper than those of degrees 5 and 15. Additionally, it is shown that at the elastic limit (i.e. $t = 0$ ka), the impact of potential stress is negligible or extremely small (differences less than 0.01), and it increases to a maximum between 2000 and 7000 yr, depending on the component considered. This highlights the low sensitivity of elastic deformation and potential, but the high sensitivity of viscous deformation and potential at the Earth's surface to the potential stress at the CMB. To summarize, the impact of potential stress at the CMB is more pronounced for low-degree (such as degree 2) viscous deformation/potential at the Earth's surface and is thus more likely to be detected through GNSS or GRACE observations of such degrees.

6.2 Solutions for a disc load example

In this section, we present the first results of a realistic loading scenario using FEMIBF. We chose FEMIBF instead of FEMIBSF because as we demonstrated in Section 6.1, the impact of the potential force at the CMB is only significant for low degree loads. We use a disc ice load of 1000 m thickness and a radius of 10°, together with a Heaviside loading history. This is the same configuration that was used in the

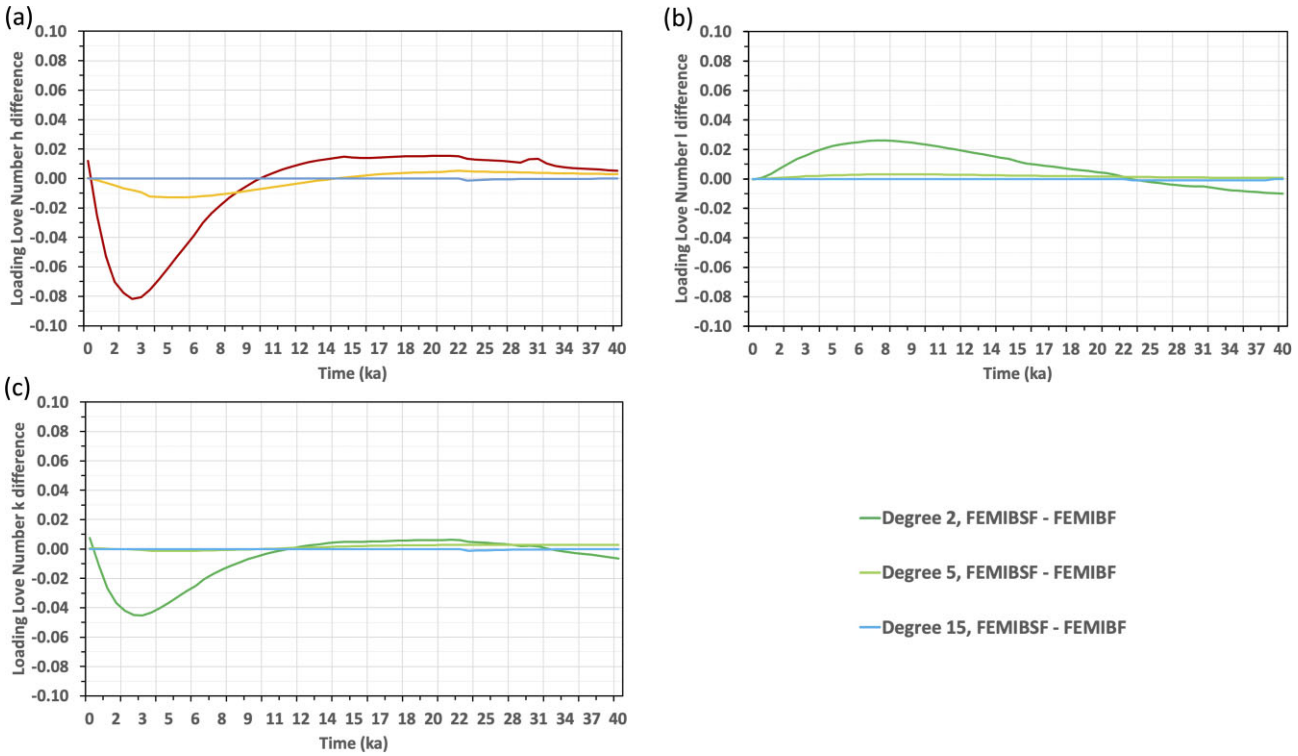

Figure 9. Love number differences between FEMIBSF and FEMIBF solutions which arise from the potential stress at the CMB.

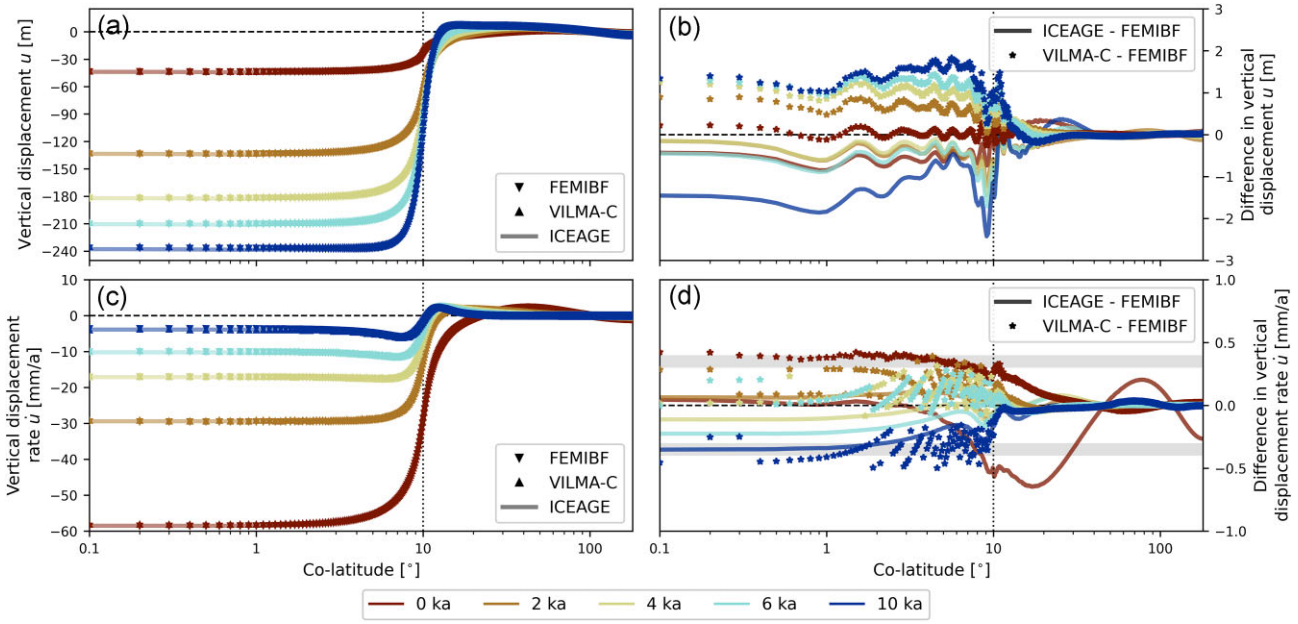

Figure 10. Comparison of the vertical displacement and its rates computed by FEMIBF with those by ICEAGE and VILMA-C. The horizontal shading lines in the panel (d) indicate the uncertainties of GNSS measurements.

incompressible GIA code benchmark by Spada *et al.* (2011, test T1/2). Our Earth model, M3-L70-V01, however, has a compressible Poisson's ratio of 0.28. FEMIBF computes the vertical, horizontal and geoid displacements, as well as their rates, at 0, 2, 4, 6 and 10 ka after Heaviside loading. To reduce computational cost while maintaining solution accuracy, FEMIBF uses adaptive meshing with a 0.25° grid spacing in the loading area and its near field, and 4° for the rest of the Earth (without vertical variations).

The results show that all three types of displacement increase in magnitude with time (between 0 and 10 ka), but their rates decrease (panels A and C of Figs 10–12). The dominant signal at all epochs is the vertical displacement rate, reaching as high as -5 mm a^{-1} at 10 ka in the loading area. The characteristics of the spatial distribution of the displacement field and its rate do not change with time, with vertical and

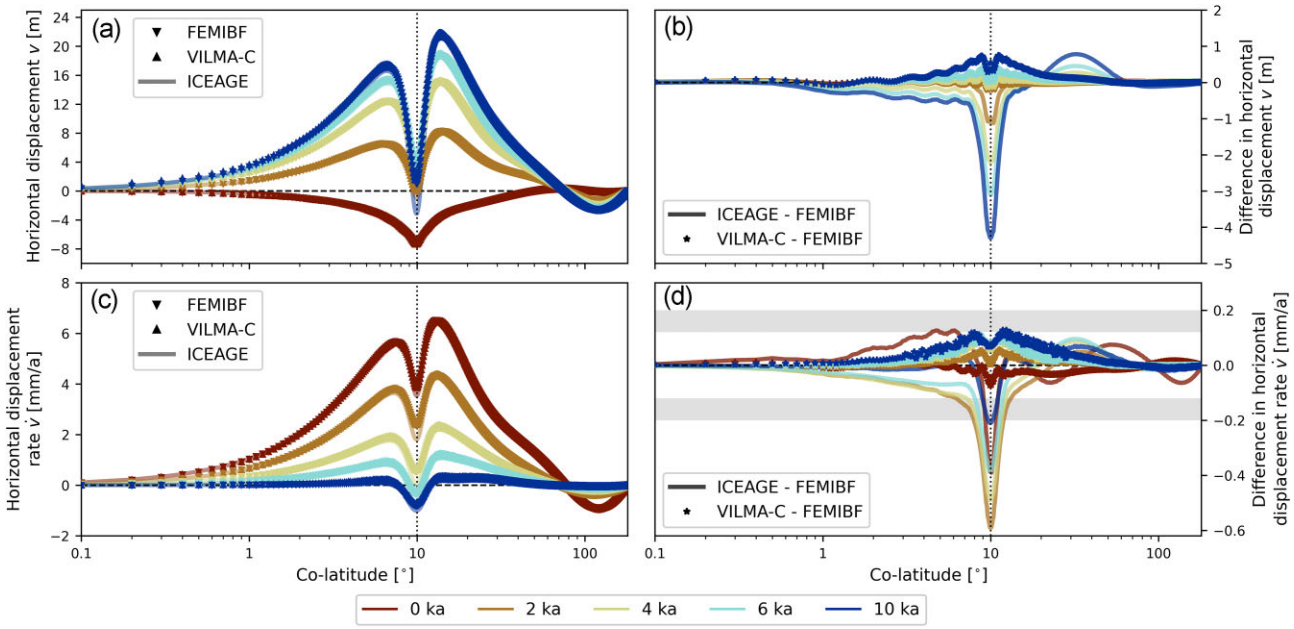

Figure 11. Same as Fig. 10 but for the horizontal displacement.

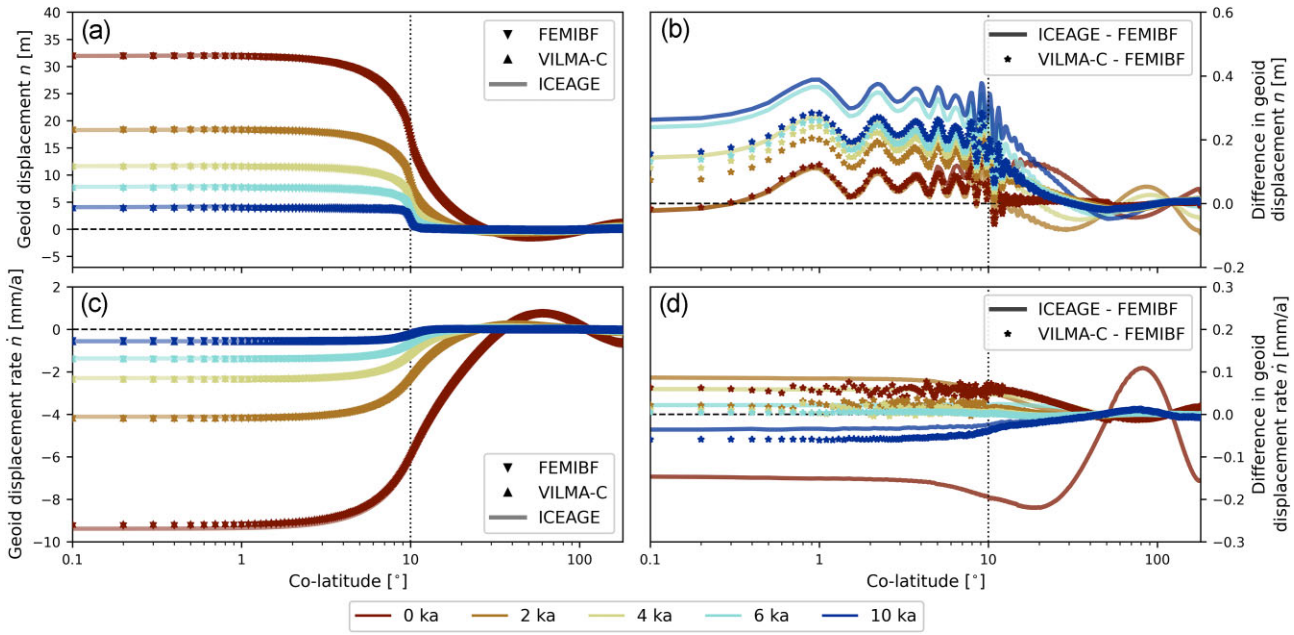

Figure 12. Same as Fig. 10 but for the geoid displacement.

geoid displacement and their rates concentrated in the loading area and horizontal displacement and its rates (virtually) symmetrical about the ice margin.

Comparison with the results generated by ICEAGE and VILMA-C reveals a satisfactory agreement (panels B of Figs 10–12), with better than 2 m for vertical displacement (<1 per cent), 4 m for horizontal displacement and 0.4 m for geoid displacement (<1 per cent). The disagreement between FEMIBF and VILMA-C results is usually smaller than that between FEMIBF and ICEAGE results. The relatively large disagreement in horizontal displacement between FEMIBF and ICEAGE occurs at the ice edge, which can be due to differences in grid representations of the load and numerical precision. Most importantly, the agreement for geoid displacement rates is better than 0.2 mm a^{-1}, and for vertical and horizontal displacement rates is mostly better than the uncertainties of GNSS measurements, being 0.4 and 0.2 mm a^{-1}, respectively (Kierulf *et al.* 2021) (panels D of Figs 10 and 12). This makes FEMIBF a suitable tool for realistic GIA loading studies of displacement rates measured by GNSS.

7 CONCLUSIONS

The new FEMIBSF method introduced here uses commercial FE packages for modelling the GIA process on a 3-D compressible, self-gravitating spherical Earth. An advantage of commercial FE packages is that they are publicly available, well tested, highly efficient and the results are highly reliable. In addition, users can easily modify it for other dedicated geophysical or geodynamic studies of large-scale Earth deformations. Our method leverages finite element techniques to calculate a range of GIA-related parameters, including dilitation, surface and body forces, radial displacement and gravitational potential. Unlike other methods that use spherical harmonics, FEMIBSF operates in the spatial domain, reducing the risk of high-degree load contributions leaking in the solution. The GIA-induced degree-1 deformation is also handled properly by FEMIBSF.

We have validated FEMIBSF by comparing results to other independently developed models and software, including the Peltier-Wu formulism, IBF, ICEAGE and VILMA-C. Our findings indicate that the accuracy of the solution is dependent on the spatial resolution, and that a non-conformal mesh with hanging nodes should be avoided.

Using FEMIBSF, we investigated the impact of the gravitational potential force from the fluid core on Earth's deformation. Our results showed that this force has a significant impact on viscous long wavelength (such as degree 2) deformation and potential at Earth's surface. Finally, we demonstrated the applicability of FEMIBSF by using it in a realistic load case and finding that the resulting vertical and horizontal displacement rates agreed with those from the two independent software ICEAGE and VILMA-C to within the uncertainty of GNSS measurements.

ACKNOWLEDGMENTS

The author PPH would like to thank Prof Zeng Pan and Prof Lei LiPing from Tsinghua University for their course 'The finite element analysis and application'. PPH was supported by GRF grant 17315316 from the Research Grants Council (RGC) in Hong Kong to PW. PPH acknowledges the funding NE/R002029/1 by NERC. PPH and VK acknowledge funding by the Helmholtz Association through the Grant ZT-0003 'Advanced Earth System Modelling Capacity—ESM' and the Federal Ministry of Education and Research (BMBF) in Germany as research for Sustainability initiative (FONA), www.fona.de through PalMod project (FKZ: 01LP1918A). RS is supported by a project grant from Rymdstyrelsen (Swedish National Space Agency; grant number 2018–00140). We acknowledge discussions with Jesse Reusen. The FE calculation was performed with the ABAQUS package from Dassault Systèmes Simulia Corp. This research is conducted in part using the research computing facilities in the Delft University of Technology.

AUTHOR CONTRIBUTIONS

PW introduced the problem to PPH. PPH developed the method, wrote the code and ran the simulations for harmonic loading, analysed the data and wrote the first draft of the manuscript. RS contributed to the figures, co-developed the formulism, wrote the code and ran the simulations for disc loading, as well as getting involved in implementing the restart function in ABAQUS, HS provided results from ICEAGE. VK provided results from VILMA-C. WVDW participated in solving the degree-1 deformation problem. PW provided the code for the Peltier-Wu formulism and the IBF code for benchmarking. YT and ZM contributed to the discussion of boundary conditions at the CMB. PPH and all co-authors made contributions to the writing of the manuscript.

DATA AVAILABILITY

The data for tested earth models's material properties and resolutions are all presented in the paper.

REFERENCES

Argus, D.F., Peltier, W.R., Blewitt, G. & Kreemer, C., 2021. The viscosity of the top third of the lower mantle estimated using GPS, GRACE, and relative sea level measurements of Glacial Isostatic Adjustment, *J. geophys. Res.,* **126**(5), e2020JB021537, doi:10.1029/2020JB021537.

Austermann, J., Hoggard, M.J., Latychev, K., Richards, F.D. & Mitrovica, J.X., 2021. The effect of lateral variations in Earth structure on Last Interglacial sea level, *Geophys. J. Int.,* **227**(3), 1938–1960.

Austermann, J., Mitrovica, J.X., Latychev, K. & Milne, G.A., 2013. Barbados-based estimate of ice volume at Last Glacial Maximum affected by subducted plate, *Nat. Geosci.,* **6**(7), 553–557.

Bängtsson, E. & Lund, B., 2008. A comparison between two solution techniques to solve the equations of glacially induced deformation of an elastic Earth, *Int. J. Numer. Methods Eng.,* **75**(4), 479–502.

Blank, B., Barletta, V., Hu, H., Pappa, F. & van der Wal, W., 2021. Effect of lateral and stress-dependent viscosity variations on GIA induced uplift rates in the Amundsen Sea Embayment, *Geochem. Geophys. Geosyst.,* **22**(9), e2021GC009807, doi:10.1029/2021GC009807.

Chinnery, M.A., 1975. The static deformation of an Earth with a fluid core: a physical approach, *Geophys. J. Int.,* **42**(2), 461–475.

Crossley, D.J. & Gubbins, D., 1975. Static deformation of the Earth's liquid core, *Geophys. Res. Lett.,* **2**(1), 1–4.

Dahlen, F.A., 1974. On the static deformation of an Earth model with a fluid core, *Geophys. J. Int.,* **36**(2), 461–485.

Dannberg, J., Eilon, Z., Faul, U., Gassmöller, R., Moulik, P. & Myhill, R., 2017. The importance of grain size to mantle dynamics and seismological observations, *Geochem. Geophys. Geosyst.,* **18**(8), 3034–3061.

Debayle, E., Bodin, T., Durand, S. & Ricard, Y., 2020. Seismic evidence for partial melt below tectonic plates, *Nature,* **586**(7830), 555–559.

Fries, T.P., Byfut, A., Alizada, A., Cheng, K.W. & Schröder, A., 2011. Hanging nodes and XFEM. *Int. J. Numer. Methods Eng.,* **86**(4-5), 404–430.

Fullea, J., Lebedev, S., Martinec, Z. & Celli, N.L., 2021. WINTERC-G: mapping the upper mantle thermochemical heterogeneity from coupled

geophysical–petrological inversion of seismic waveforms, heat flow, surface elevation and gravity satellite data, *Geophys. J. Int.,* **226**(1), 146–191.
Gasperini, P. & Sabadini, R., 1989. Lateral heterogeneities in mantle viscosity and post-glacial rebound, *Geophys. J. Int.,* **98**(3), 413–428.
Geruo, A., Wahr, J. & Zhong, S., 2013. Computations of the viscoelastic response of a 3-D compressible Earth to surface loading: an application to Glacial Isostatic Adjustment in Antarctica and Canada, *Geophys. J. Int,* **192,** 557–572.
Gomez, N., Latychev, K. & Pollard, D., 2018. A coupled ice sheet–sea level model incorporating 3D Earth structure: variations in Antarctica during the last deglacial retreat, *J. Clim.,* **31**(10), 4041–4054.
Gomez, N., Mitrovica, J.X., Huybers, P. & Clark, P.U., 2010. Sea level as a stabilizing factor for marine-ice-sheet grounding lines, *Nat. Geosci.,* **3**(12), 850–853.
Hampel, A., Lüke, J., Krause, T. & Hetzel, R., 2019. Finite-element modelling of glacial isostatic adjustment (GIA): use of elastic foundations at material boundaries versus the geometrically non-linear formulation, *Comput. Geosci.,* **122,** 1–14.
Hanyk, L., Matyska, C. & Yuen, D.A., 1999. Secular gravitational instability of a compressible viscoelastic sphere, *Geophys. Res. Lett.,* **26**(5), 557–560.
Hanyk, L., Matyska, C. & Yuen, D.A., 2005. Short time-scale heating of the Earth's mantle by ice-sheet dynamics, *Earth, Planets Space,* **57**(9), 895–902.
Hanyk, L., Yuen, D.A. & Matyska, C., 1996. Initial-value and modal approaches for transient viscoelastic responses with complex viscosity profiles, *Geophys. J. Int.,* **127**(2), 348–362.
Haskell, N.A., 1935. The motion of a viscous fluid under a surface load, *Physics,* **6,** 265–369.
Hu, H., van der Wal, W. & Vermeersen, L.L.A., 2017. A numerical method for reorientation of rotating tidally deformed viscoelastic bodies, *J. geophys. Res.,* **122**(1), 228–248.
Huang, P., Sulzbach, R.L., Klemann, V., Tanaka, Y., Dobslaw, H., Martinec, Z. & Thomas, M., 2022. The influence of sediments, lithosphere and upper mantle (anelastic) with lateral heterogeneity on ocean tide loading and ocean tide dynamics, *J. geophys. Res.,* **127**(11), doi:10.1029/2022JB025200.
Huang, P., Sulzbach, R.L., Tanaka, Y., Klemann, V., Dobslaw, H., Martinec, Z. & Thomas, M., 2021. Anelasticity and lateral heterogeneities in Earth's upper mantle: impact on surface displacements, self-attraction and loading and ocean tide dynamics, *J. geophys. Res.,* **126**(9), e2021JB022332, doi:10.1029/2021JB022332.
Huang, P., Wu, P. & Steffen, H., 2019. In search of an ice history that is consistent with composite rheology in Glacial Isostatic Adjustment modelling. *Earth planet. Sci. Lett.,* **517,** 26–37.
Huang, P., Wu, P. & van der Wal, W., 2018. Effects of mantle rheologies on viscous heating induced by Glacial Isostatic Adjustment, *Geophys. J. Int.,* **213**(1), 157–168.
Karaoğlu, H. & Romanowicz, B., 2018. Inferring global upper-mantle shear attenuation structure by waveform tomography using the spectral element method, *Geophys. J. Int.,* **213**(3), 1536–1558.
Karato, S.I. & Wu, P., 1993. Rheology of the upper mantle: a synthesis, *Science,* **260**(5109), 771–778.
Kaufmann, G., 2004. *Program Package ICEAGE, Version 2004,* Institut für Geophysik der Universität Göttingen.
Kaufmann, G. & Lambeck, K., 2000. Mantle dynamics, postglacial rebound and the radial viscosity profile, *Phys. Earth planet. Inter.,* **121**(3-4), 301–324.
Kaufmann, G. & Lambeck, K., 2002. Glacial isostatic adjustment and the radial viscosity profile from inverse modeling, *J. geophys. Res.,* **107**(B11), ETG–5.
Kaufmann, G., Wu, P. & Wolf, D., 1997. Some effects of lateral heterogeneities in the upper mantle on postglacial land uplift close to continental margins, *Geophys. J. Int.,* **128**(1), 175–187.
Kierulf, H.P., Steffen, H., Barletta, V.R., Lidberg, M., Johansson, J., Kristiansen, O. & Tarasov, L., 2021. A GNSS velocity field for geophysical applications in Fennoscandia, *J. Geodyn.,* **146,** doi:10.1016/j.jog.2021.101845.
Klemann, V. & Martinec, Z., 2011. Contribution of glacial-isostatic adjustment to the geocenter motion, *Tectonophysics,* **511,** 99–108.
Klemann, V., Martinec, Z. & Ivins, E.R., 2008. Glacial isostasy and plate motions, *J. Geodyn.,* **46,** 95–103.
Klemann, V., Wu, P. & Wolf, D., 2003. Compressible viscoelasticity: stability of solutions for homogeneous plane-Earth models, *Geophys. J. Int.,* **153,** 569–585.
Lambeck, K., Purcell, A. & Zhao, S., 2017. The North American Late Wisconsin ice sheet and mantle viscosity from glacial rebound analyses, *Quat. Sci. Rev.,* **158,** 172–210.
Latychev, K., Mitrovica, J.X., Tromp, J., Tamisiea, M.E., Komatitsch, D. & Christara, C.C., 2005. Glacial isostatic adjustment on 3-D Earth models: a finite-volume formulation, *Geophys. J. Int.,* **161**(2), 421–444.
Lau, H.C., Mitrovica, J.X., Austermann, J., Crawford, O., Al-Attar, D. & Latychev, K., 2016. Inferences of mantle viscosity based on ice age data sets: radial structure, *J. geophys. Res.,* **121**(10), 6991–7012.
Li, T. *et al.*, 2022. Influence of 3D Earth structure on Glacial Isostatic Adjustment in the Russian Arctic, *J. geophys. Res.,* **127**(3), e2021JB023631, doi:10.1029/2021JB023631.
Li, T., Wu, P., Steffen, H. & Wang, H., 2018. In search of laterally heterogeneous viscosity models of glacial isostatic adjustment with the ICE-6G_C global ice history model, *Geophys. J. Int.,* **214**(2), 1191–1205.
Martinec, Z., 2000. Spectral–finite element approach to three-dimensional viscoelastic relaxation in a spherical Earth, *Geophys. J. Int.,* **142**(1), 117–141.
Martinec, Z. & Hagedoorn, J., 2005. Time-domain approach to linearized rotational response of a three-dimensional viscoelastic earth model induced by glacial-isostatic adjustment: I. Inertia-tensor perturbations, *Geophys. J. Int.,* **163**(2), 443–462.
Martinec, Z. & Hagedoorn, J., 2014. The rotational feedback on linear-momentum balance in glacial isostatic adjustment, *Geophys. J. Int.,* **199**(3), 1823–1846.
Mitrovica, J.X., Wahr, J., Matsuyama, I. & Paulson, A., 2005. The rotational stability of an ice-age Earth, *Geophys. J. Int.,* **161**(2), 491–506.
Paulson, A., Zhong, S. & Wahr, J., 2005. Modelling post-glacial rebound with lateral viscosity variations, *Geophys. J. Int.,* **163**(1), 357–371.
Peltier, W.R., 1974. The impulse response of a Maxwell Earth, *Rev. Geophys.,* **12**(4), 649–669.
Peltier, W.R., 1998. Postglacial variations in the level of the sea: implications for climate dynamics and solid-earth geophysics, *Rev. Geophys.,* **36**(4), 603–689.
Peltier, W.R., 2004. Global glacial isostasy and the surface of the ice-age Earth: the ICE-5 G (VM2) model and GRACE, *Annu. Rev. Earth Planet. Sci.,* **32,** 111–149.
Peltier, W.R., Argus, D.F. & Drummond, R., 2015. Space geodesy constrains ice age terminal deglaciation: the global ICE-6G_C (VM5a) model, *J. geophys. Res.,* **120**(1), 450–487.
Peltier, W.R., Wu, P.P.C., Argus, D., Li, T. & Velay-Vitow, J., 2022. Glacial isostatic adjustment: physical models and observational constraints, *Rep. Prog. Phys.,* **85**(9), doi:10.1088/1361-6633/ac805b.
Plag, H.-P. & Jüttner, H.-U., 1995. Rayleigh-Taylor instabilities of a self-gravitating Earth, *J. Geodyn.,* **20,** 267–288.
Priestley, K., McKenzie, D. & Ho, T., 2018. A lithosphere–asthenosphere boundary—a global model derived from multimode surface-wave tomography and petrology, in *Lithospheric Discontinuities,* Chapter 6, Geophysical Monograph Series, pp. 111–123, eds Yuan, H. & Romanowicz, B., AGU.
Reusen, J.M., Steffen, R., Steffen, H., Root, B.C. & van der Wal, W., 2023. Simulating horizontal crustal motions of glacial isostatic adjustment using compressible Cartesian models, *Geophys. J. Int.,* **235**(1), 542–553.
Schaeffer, A.J. & Lebedev, S., 2013. Global shear speed structure of the upper mantle and transition zone, *Geophys. J. Int.,* **194**(1), 417–449.
Smylie, D.E. & Mansinha, L., 1971. The elasticity theory of dislocations in real Earth models and changes in the rotation of the Earth, *Geophys. J. Int.,* **23**(3), 329–354.
Spada, G., Barletta, V.R., Klemann, V., Riva, R.E.M., Martinec, Z., Gasperini, P. & King, M.A., 2011. A benchmark study for glacial isostatic adjustment codes, *Geophys. J. Int.,* **185**(1), 106–132.

Steffen, H., Kaufmann, G. & Wu, P., 2006. Three-dimensional finite-element modeling of the glacial isostatic adjustment in Fennoscandia, *Earth Planet. Sci. Lett.,* **250**(1–2), 358–375.
Steffen, H. & Wu, P., 2011. Glacial isostatic adjustment in Fennoscandia—a review of data and modeling, *J. Geodyn.,* **52**(3-4), 169–204.
Steffen, R., Wu, P., Steffen, H. & Eaton, D.W., 2014. On the implementation of faults in finite-element glacial isostatic adjustment models, *Comput. Geosci.,* **62,** 150–159.
Tanaka, Y., Klemann, V., Martinec, Z. & Riva, R.E.M., 2011. Spectral-finite element approach to viscoelastic relaxation in a spherical compressible Earth: application to GIA modelling, *Geophys. J. Int.,* **184**(1), 220–234.
Tanaka, Y., Klemann, V. & Okuno, J., 2009. Application of a numerical inverse Laplace integration method to surface loading on a viscoelastic compressible Earth model, *Pure appl. Geophys.,* **166**(8-9), 1199–1216.
Tromp, J. & Mitrovica, J.X., 1999. Surface loading of a viscoelastic Earth—I. General theory, *Geophys. J. Int.,* **137**(3), 847–855.
Tromp, J. & Mitrovica, J.X., 2000. Surface loading of a viscoelastic planet—III. Aspherical models, *Geophys. J. Int.,* **140**(2), 425–441.
Vermeersen, L.L.A. & Mitrovica, J.X., 2000. Gravitational stability of spherical self-gravitating relaxation models, *Geophys. J. Int.,* **142**(2), 351–360.
Wang, Y. & Li, M., 2021. The interaction between mantle plumes and lithosphere and its surface expressions: 3-D numerical modelling, *Geophys. J. Int.,* **225**(2), 906–925.
Whitehouse, P.L., 2018. Glacial isostatic adjustment modelling: historical perspectives, recent advances, and future directions, *Earth Surf. Dyn.,* **6**(2), 401–429.
Wong, M.C. & Wu, P., 2019. Using commercial finite-element packages for the study of Glacial Isostatic Adjustment on a compressible self-gravitating spherical Earth–1: harmonic loads, *Geophys. J. Int.,* **217**(3), 1798–1820.
Wu, P., 1992. Deformation of an incompressible viscoelastic flat earth with powerlaw creep: a finite element approach, *Geophys. J. Int.,* **108**(1), 35–51.
Wu, P., 1993. Postglacial rebound in a power-law medium with axial symmetry and the existence of the transition zone in relative sea-level data, *Geophys. J. Int.,* **114**(3), 417–432.
Wu, P., 2004. Using commercial finite element packages for the study of Earth deformations, sea levels and the state of stress, *Geophys. J. Int.,* **158**(2), 401–408.
Wu, P. & Mazzotti, S., 2007. Effects of a lithospheric weak zone on post-glacial seismotectonics in Eastern Canada and Northeastern USA, in *Continental Intraplate Earthquakes: Science, Hazard, and Policy Issues,* pp. 113–128, eds Stein, S. & Mazzotti, S., GSA Special Paper 425, Geological Society of America.
Wu, P. & Peltier, W.R., 1982. Viscous gravitational relaxation, *Geophys. J. Int.,* **70**(2), 435–485.
Wu, P. & Peltier, W.R., 1984. Pleistocene deglaciation and the Earth's rotation: a new analysis, *Geophys. J. Int.,* **76**(3), 753–791.
Wu, P., Steffen, R., Steffen, H. & Lund, B., 2022. Glacial Isostatic Adjustment models for earthquake triggering, in *Glacially-Triggered Faulting,* pp. 383–401, eds Steffen, H., Olessen, O. & Sutinen, R., Cambridge Univ. Press.
Wu, P. & van der Wal, W., 2003. Postgcelacial sealevels on a spherical, self-gravitating viscoelastic Earth: effects of lateral viscosity variations in the upper mantle on the inference of viscosity contrasts in the lower mantle, *Earth planet. Sci. Lett.,* **211,** 57–68.
Wu, P., Wang, H. & Schotman, H., 2005. Postglacial induced surface motions, sea-levels and geoid rates on a spherical, self-gravitating laterally heterogeneous earth, *J. Geodyn.,* **39**(2), 127–142.
Yousefi, M., Milne, G.A. & Latychev, K., 2021. Glacial isostatic adjustment of the Pacific Coast of North America: the influence of lateral Earth structure, *Geophys. J. Int.,* **226**(1), 91–113.
Zhong, S., Paulson, A. & Wahr, J., 2003. Three-dimensional finite-element modelling of Earth's viscoelastic deformation: effects of lateral variations in lithospheric thickness, *Geophys. J. Int.,* **155**(2), 679–695.
Zienkiewicz, O.C., Taylor, R.L. & Zhu, J.Z., 2005. *The Finite Element Method: Its Basis and Fundamentals,* Elsevier.

APPENDIX A: CLASSICAL FINITE ELEMENT EQUATIONS ADOPTED BY FEMIBSF TO DO INTERPOLATION, INTEGRATION AND COMPUTE GEOMETRIC AREA AND VOLUME

The earth model considered here is spherical and made up of 3-D brick elements with 8 nodes (of the type C3D8 in ABAQUS). For the kth physical element L_k (Fig. A1), points 1–4 and 5–8 construct a lower and upper surface, respectively, with the same radius (r) but different colatitude (θ) and longitude (φ). Some of these surfaces are where the driving forces of GIA such as the loading and supporting pressures on Earth's surface and core–mantle boundary (CMB), respectively, are applied. The spherical coordinates for points 1–8 can be transformed into Cartesian coordinates (x_i, y_i, z_i) $(i = 1, 8)$, which are then mapped to the coordinates of a first-order isoparametric element R_k (Fig. A1) with points 1–8 mapped to points 1′–8′ successively. The purpose of such mapping is to move the complex calculations in the physical element L_k to the standard and easier calculations in the isoparamtric element R_k, which will be shown in the following.

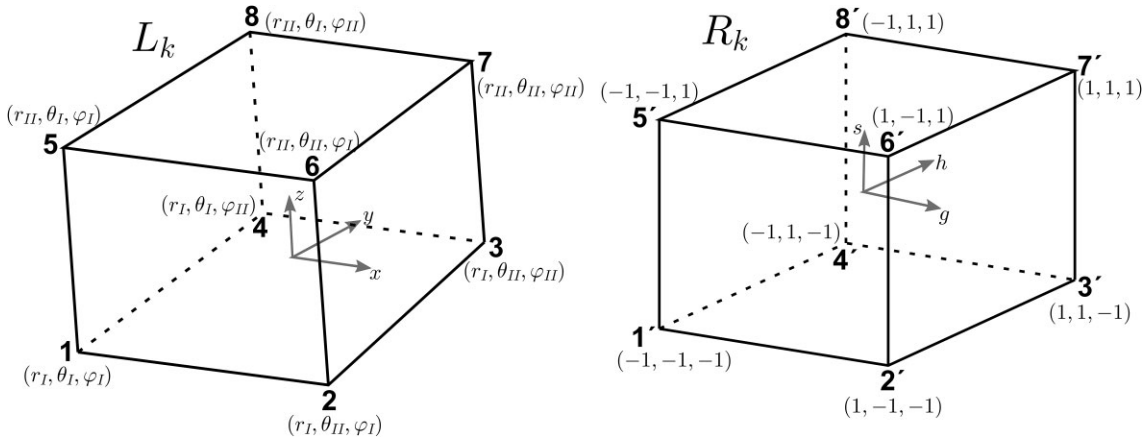

Figure A1: Configuration of the kth element.

Let (g_i, h_i, s_i) be the coordinates of points 1′–8′ in R_k with $g_i = \pm 1$, $h_i = \pm 1$ and $s_i = \pm 1$ $(i = 1, 8)$. It follows that (e.g. Zienkiewicz *et al.* 2005) the point (x, y, z) within L_k can be interpolated by

$$\begin{aligned} x(g,h,s) &= \sum_{i=1}^{8} N_i(g,h,s)\, x_i, \\ y(g,h,s) &= \sum_{i=1}^{8} N_i(g,h,s)\, y_i, \\ z(g,h,s) &= \sum_{i=1}^{8} N_i(g,h,s)\, z_i, \end{aligned} \tag{A1}$$

where the ith shape function is known as

$$N_i(g,h,s) = \frac{1}{8}(1+g_i g)(1+h_i h)(1+s_i s). \tag{A2}$$

This interpolation method is identical to the so-called trilinear interpolation. The derivatives of x, y and z with respect to g, h and s simply read

$$\begin{aligned} \frac{\partial x}{\partial g/h/s} &= \sum_{i=1}^{8} \frac{\partial N_i}{\partial g/h/s} x_i, \\ \frac{\partial y}{\partial g/h/s} &= \sum_{i=1}^{8} \frac{\partial N_i}{\partial g/h/s} y_i, \\ \frac{\partial z}{\partial g/h/s} &= \sum_{i=1}^{8} \frac{\partial N_i}{\partial g/h/s} z_i. \end{aligned} \tag{A3}$$

This set of equations can be used now to calculate the surface area and element volume which further facilitate the calculation of average surface and body forces. Let the infinitesimal surface area on L_k, for example on the 5–6–7–8 plane, be denoted by dS. This area can be mapped to a surface area d$S' =$ dgdh on the 5′–6′–7′–8′ plane of R_k through

$$\mathrm{d}S = \|Js\|\mathrm{d}g\,\mathrm{d}h = \sqrt{\left(\|J_{S,xy}\|^2 + \|J_{s,yz}\|^2 + \|J_{s,zx}\|^2\right)}\,\mathrm{d}g\,\mathrm{d}h, \tag{A4}$$

where the Jacobian matrices are given by

$$J_{S,xy} = \begin{bmatrix} \frac{\partial x}{\partial g} & \frac{\partial y}{\partial g} \\ \frac{\partial x}{\partial h} & \frac{\partial y}{\partial h} \end{bmatrix}, \quad J_{S,yz} = \begin{bmatrix} \frac{\partial y}{\partial g} & \frac{\partial z}{\partial g} \\ \frac{\partial y}{\partial h} & \frac{\partial z}{\partial h} \end{bmatrix}, \quad J_{S,zx} = \begin{bmatrix} \frac{\partial z}{\partial g} & \frac{\partial x}{\partial g} \\ \frac{\partial z}{\partial h} & \frac{\partial x}{\partial h} \end{bmatrix}. \tag{A5}$$

Note that $||J_{S,xy}||$, $||J_{S,yz}||$ and $||J_{S,zx}||$ are absolute values of the determinants of $J_{S,xy}$, $J_{S,yz}$ and $J_{S,zx}$, respectively. Due to mapping, calculating the surface area S_k of element L_k is done in the reference frame R_k with

$$S_k = \int_{-1}^{1}\int_{-1}^{1} \|J_S\|\,\mathrm{d}g\,\mathrm{d}h\,, \tag{A6}$$

which is then evaluated with the two-point Gauss–Legendre quadrature rule by

$$S_k \cong \sum_{j=1}^{4} \|J_S(h_j, g_j, 1)\| = \sum \|J_S\left(\pm\frac{1}{\sqrt{3}}, \pm\frac{1}{\sqrt{3}}, 1\right)\|. \tag{A7}$$

Similarly, the infinitesimal volume dV in L_k can be mapped through

$$\mathrm{d}V = \|J_V\|\,\mathrm{d}h\,\mathrm{d}g\,\mathrm{d}s, \tag{A8}$$

where the Jacobian matrix is

$$J_V = \begin{bmatrix} \frac{\partial x}{\partial g} & \frac{\partial y}{\partial g} & \frac{\partial z}{\partial g} \\ \frac{\partial x}{\partial h} & \frac{\partial y}{\partial h} & \frac{\partial z}{\partial h} \\ \frac{\partial x}{\partial s} & \frac{\partial y}{\partial s} & \frac{\partial z}{\partial s} \end{bmatrix}. \tag{A9}$$

The volume of L_k is again calculated on R_k by

$$V_k \cong \sum_{j=1}^{8} \|J_V(h_j, g_j, s_j)\| = \sum \|J_V\left(\pm\frac{1}{\sqrt{3}}, \pm\frac{1}{\sqrt{3}}, \pm\frac{1}{\sqrt{3}}\right)\|, \tag{A10}$$

using the same two-point Gauss–Legendre quadrature rule.

APPENDIX B: THE FE METHOD OF INTERPOLATING RADIAL DISPLACEMENTS

The GIA-induced radial displacement across a density jump needs to be specifically treated. The proposed approach here uses ABAQUS to solve the equation of equilibrium for GIA (Section 2.3) with the Cartesian displacements of all 8 nodes of each element as one of the outputs (Appendix A). Taking advantage of this nodal output for element L_k (Fig. A1), we interpolate the displacement within the element in the R_k frame (Fig. A1), similar to the interpolation of coordinates, by

$$\begin{aligned} u_x &= \sum_{i=1}^{8} N_i(g,h,s)\ u_{xi}, \\ u_y &= \sum_{i=1}^{8} N_i(g,h,s)\ u_{yi}, \\ u_z &= \sum_{i=1}^{8} N_i(g,h,s)\ u_{zi}, \end{aligned} \tag{B1}$$

where u_{xi}, u_{yi} and u_{zi} are nodal displacements in the x, y and z direction of element L_k, respectively, while u_x, u_y and u_z are displacements within the element R_k with directions g, h and s. It follows that the derivative of u_x, u_y and u_z with respect to g, h and s are

$$\begin{aligned} \frac{\partial u_x}{\partial g/h/s} &= \sum_{i=1}^{8} \frac{\partial N_i}{\partial g/h/s}\ u_{xi}, \\ \frac{\partial u_y}{\partial g/h/s} &= \sum_{i=1}^{8} \frac{\partial N_i}{\partial g/h/s}\ u_{yi}, \\ \frac{\partial u_z}{\partial g/h/s} &= \sum_{i=1}^{8} \frac{\partial N_i}{\partial g/h/s}\ u_{zi}. \end{aligned} \tag{B2}$$

Applying the transformation rule on vectors between the spherical and Cartesian coordinate system, one can obtain the radial displacement as

$$u_r = \frac{x\ u_x}{r} + \frac{y\ u_y}{r} + \frac{z\ u_z}{r}. \tag{B3}$$

Differentiating u_r in R_k and making use of eq. (A1), one can get

$$\begin{bmatrix} \frac{\partial u_r}{\partial g} \\ \frac{\partial u_r}{\partial h} \\ \frac{\partial u_r}{\partial s} \end{bmatrix} = J_V \begin{bmatrix} \frac{u_x}{r} - \frac{x u_r}{r^2} \\ \frac{u_y}{r} - \frac{y u_r}{r^2} \\ \frac{u_z}{r} - \frac{z u_r}{r^2} \end{bmatrix} + \begin{bmatrix} \frac{\partial u_x}{\partial g} & \frac{\partial u_y}{\partial g} & \frac{\partial u_z}{\partial g} \\ \frac{\partial u_x}{\partial h} & \frac{\partial u_y}{\partial h} & \frac{\partial u_z}{\partial h} \\ \frac{\partial u_x}{\partial s} & \frac{\partial u_y}{\partial s} & \frac{\partial u_z}{\partial s} \end{bmatrix} \begin{bmatrix} \frac{x}{r} \\ \frac{y}{r} \\ \frac{z}{r} \end{bmatrix}, \tag{B4}$$

where J_V is the volumetric Jacobian matrix given in eq. (A9). Alternatively, one can interpolate the radial displacement and its derivative within the element by

$$u_r = \sum_{i=1}^{8} N_i(g,h,s)\ u_{ri} \tag{B5}$$

and

$$\frac{\partial u_r}{\partial g} = \sum_{i=1}^{8} \frac{\partial N_i}{\partial g}\ u_{ri}, \quad \frac{\partial u_r}{\partial h} = \sum_{i=1}^{8} \frac{\partial N_i}{\partial h}\ u_{ri}, \quad \frac{\partial u_r}{\partial s} = \sum_{i=1}^{8} \frac{\partial N_i}{\partial s}\ u_{ri}. \tag{B6}$$

APPENDIX C: POTENTIAL IMPLEMENTATION OF GIA ROTATIONAL FEEDBACK WITH FEMIBSF

GIA causes perturbations of Earth's moments of inertia which further affect the angular velocities of Earth's rotation. This directly leads to changes in the length of day and polar wander of the rotational pole (Wu & Peltier 1984; Martinec & Hagedoorn 2005; Mitrovica *et al.* 2005; Paulson *et al.* 2005; Geruo *et al.* 2013; Peltier *et al.* 2022). Moreover, it raises an additional centrifugal potential Λ (Wu & Peltier 1984; Mitrovica *et al.* 2005; Martinec & Hagedoorn 2014) which has consequences on the equilibrium equation of GIA (eq. 2.3.1) and the sea level equation (SLE).

When implementing the rotational feedback with FEMIBSF, first the change in moment of inertia needs to be calculated (*cf.* Hu *et al.* 2017) from which the angular velocity, polar wander, length of day and centrifugal potential follow. Then, the centrifugal potential Λ needs to be added to the perturbed gravitational potential ϕ_1 in eq. (2.3.1). This will introduce a centrifugal force to each FE body of the solid Earth and so induce additional deformations and gravitational potential changes, which induces a change in moment of inertia and hence a new angular velocity. Therefore, an iteration for each time step as done in the FEMIBSF is required to calculate these rotational feedbacks. In addition, 3-D viscosity can have a strong effect on the moment of inertia of the surface loading and its deformation. This impact has to be considered in calculating rotational feedbacks for a laterally heterogeneous Earth.

The SLE with rotational feedback can be included with FEMIBSF method as well. For realistic time and space dependent surface ice and ocean loads, the regular SLE (without rotational feedback) at the Earth's surface and (θ, ϕ, t) is given by (e.g. Wu 2004):

$$S(\theta,\phi,t) = \left[\frac{\phi_1(\theta,\phi,t)}{g} - U(\theta,\phi,t) + c(t)\right] O_n(\theta,\phi,t), \tag{C1}$$

where $c(t) = -\frac{M_I(t)}{\rho_w A_o(t)} - \frac{1}{A_o(t)}\langle \frac{\phi_1}{g} - U\rangle_{\text{ocean}}$, and $U(\theta,\phi,t)$, $\phi_1(\theta,\phi,t)$, $O_n(\theta,\phi,t)$, $A_o(t)$, $M_I(t)$, ρ_w, g are the radial displacement and the perturbed gravitational potential, the time-dependent Ocean Function, the area of the ocean basins, the mass loss history of the ice, the density of water, gravitational constant at the Earth's surface, respectively, and $< >_{\text{ocean}}$ represents integration over the ocean basins. The changing water load $S(\theta,\phi,t) * \rho_w$ can be updated iteratively as surface load σ in oceans (see Section 2.3.3) in FEMIBSF. The inclusion of rotational feedback in the SLE is important for sea level studies but the computation can be a little burdensome for a 3-D Earth (see Paulson *et al.* 2005; Geruo *et al.* 2013). However, the degree-2 component of lateral heterogeneity from seismic tomographic models or nonlinear rheology is weak, so mode coupling can be neglected. That means rotational feedback can be computed in the same way as for a laterally homogeneous Earth (e.g. Li *et al.* 2018). The equation for the computation of the SLE with rotational feedback is:

$$S(\theta,\phi,t) = \left[\frac{\phi_1(\theta,\phi,t)}{g} - U(\theta,\phi,t) + G^T \otimes \Lambda + c(t)\right] O_n, \tag{C2}$$

where $c(t) = -\frac{M_I(t)}{\rho_w A_o(t)} - \frac{1}{A_o(t)}\langle \frac{\phi_1}{g} - U + G^T \otimes \Lambda\rangle_{\text{ocean}}$. Comparing with the above eq. (C1) for regular SLE, the extra term $G^T \otimes \Lambda$ is the tidal or rotation-induced sea level change and can be obtained by convoluting $\Lambda(\theta,\phi,t)$, the perturbed rotational/centrifugal potential, with G^T, the Green's function for tidal induced sea level change (e.g. Peltier *et al.* 2022). The SLE with rotational feedback can be solved using the same iterative procedure for the regular SLE, except the extra rotational feedback term is included. The details of adding rotational feedback in FEMIBSF can be found in sections 4.2 and 6.6 of Peltier *et al.* (2022).